

## Friction Welding of a Rapidly Solidified Al-Fe-V-Si Alloy

*Metallurgical characteristics of inertia and linear friction welds in an advanced aluminum alloy were comparatively evaluated in similar and dissimilar joints*

BY H. H. KOO AND W. A. BAESLACK III

**ABSTRACT.** Inertia and linear friction welds produced in a rapidly solidified/powder metallurgy Al-Fe-V-Si alloy have been investigated from a metallurgical perspective. Similar-alloy welds in Al-11.7 wt-% Fe-1.2 wt-% V-2.4 wt-% Si (hereafter designated as FVS1212) and dissimilar-alloy welds between FVS1212 and ingot metallurgy 2024-T351 were generated and characterized using light and analytical-electron microscopy, mechanical testing and fractographic analysis.

The application of a relatively high axial force during inertia friction welding was found to be critical in promoting sufficient expulsion of severely heat- and deformation-affected metal out of the weld interface region, thereby maintaining a fine dispersoid and alpha grain size in the weld zone and achieving a high joint efficiency (85%). Although linear friction welds in FVS1212 exhibited a greater extent of dispersoid coarsening in the weld zone due to a comparatively slower thermal cycle and lower degree of expulsion, only a slight decrease in joint efficiency (down to 80%) was measured vs. the optimum inertia friction welds. Consistent with hardness and tensile test data, fractographic analysis of tensile and three-point bend specimen surfaces using scanning-electron microscopy revealed fracture to occur at the center of the heat- and deformation-affected zones in all similar alloy welds.

W. A. BAESLACK III is a Professor and H. H. KOO is a Research Associate, Department of Welding Engineering, The Ohio State University, Columbus, Ohio.

Light and analytical electron microscopy analysis of the dissimilar-alloy friction welds showed microstructural changes to occur predominantly in the 2024-T351. These changes included severe deformation and reorientation of the base metal alpha grains, reversion and/or solutionizing of the strengthening precipitates, and the promotion of dynamic recrystallization directly adjacent to the weld interface. Mechanical mixing between the alloys was limited to an extremely narrow region across the weld interface, and was less extensive in the linear friction vs. the inertia friction welds. Results of the hardness traverses correlated closely with microstructural features, showing a hardness decrease in the 2024-T351 heat- and deformation-affected zone but no change in the FVS1212. Transverse-weld tensile test results showed high joint efficiencies of 95 and 86% (based on the 2024-T351 base metal strength) for the high axial force inertia friction and linear friction welds, respectively.

Scanning electron microscopy/energy-dispersive x-ray fractographic anal-

ysis of both tensile and three-point bend specimens showed fracture to occur along the weld interface, or within the 2024-T351 or FVS1212 directly adjacent to this interface. The proportion of fracture directly along the interface was most extensive near the outer periphery vs. the center of both the inertia friction and linear friction welds.

The present study has demonstrated feasibility of both the inertia and linear friction welding processes for the effective solid-state joining of FVS1212, and has determined process effects on the joint structure and mechanical properties. It is anticipated that further process parameter optimization, particularly for the linear friction welding process, would result in further improvements in joint properties.

### Introduction

Recent advances in rapid solidification (RS) technology have led to the development of a new generation of high-strength aluminum alloys for elevated-temperature applications up to 375°C (707°F) (Refs. 1-4). These alloys are based on hypereutectic Al-Fe-based compositions (8.5-12 wt-% Fe) with lesser ternary and quaternary additions of vanadium and silicon. Through RS processing, a unique, "engineered" microstructure is obtained which consists of a high volume fraction of nearly spherical, submicron  $\text{Al}_{13}(\text{Fe},\text{V})_3$  Si dispersoids (body-centered cubic) in an extremely fine-grained alpha aluminum matrix (Ref. 2). The low interfacial energy between the dispersoid particles

### KEY WORDS

Dispersion-Hardened Alloy  
RS/PM Alloy  
Al-Fe-V-Si  
2024-T351  
Inertia Friction Welding  
Linear Friction Welding  
Similar-Alloy Welds  
Dissimilar-Alloy Welds

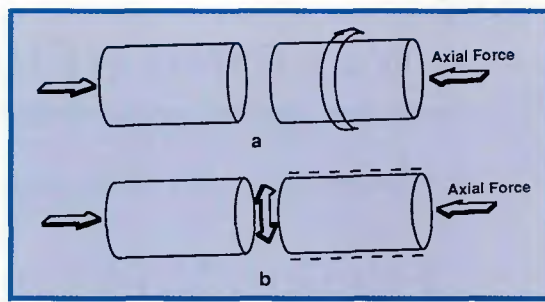
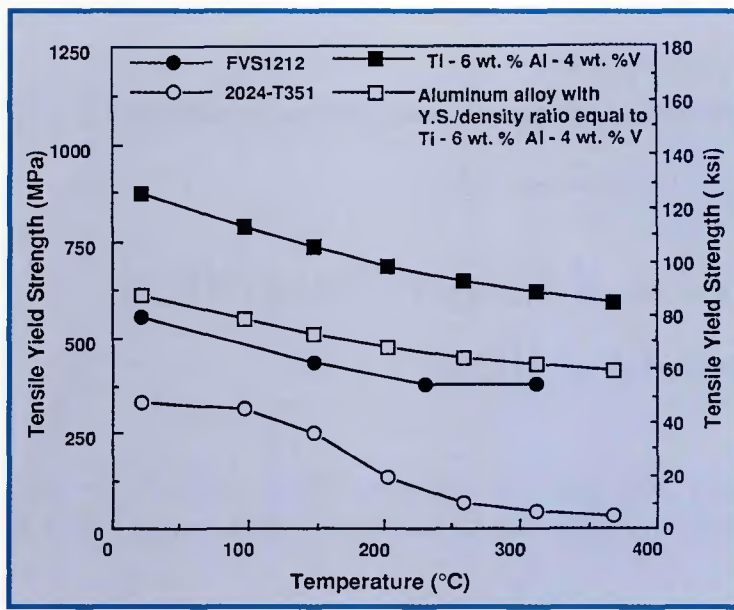


Fig. 2 — Schematic representations. A — Inertia friction welding process; B — linear friction welding process.

Fig. 1 — A comparison of tensile yield strength vs. test temperature for FVS1212, 2024-T351 and Ti-6 wt-% Al- 4 wt-% V (Refs. 1 and 15).

and the matrix and the low solid-state diffusivity and solubility of the transition metal alloying elements in alpha aluminum minimize the driving force for particle coarsening, thereby promoting their stability at temperatures up to 375°C. These microstructural features provide high room-temperature strength and excellent elevated temperature mechanical properties, in contrast to conventional high-strength aluminum alloys which rapidly lose their strength above 150°C (302°F) due to coarsening of the strengthening precipitates. As shown in Fig. 1, the Al-Fe-V-Si alloys exhibit specific strengths comparable to Ti-6 wt-% Al-4 wt-% V up to 375°C (Ref. 2). The spherical morphology of  $\text{Al}_{13}(\text{Fe}, \text{V})_3\text{Si}$  and absence of acicular  $\text{Al}_3\text{Fe}$  (monoclinic) dispersoids further promote excellent ductility, fracture toughness and fatigue properties comparable to those of conventional high-strength aluminum alloys. Consequently, RS Al-Fe-V-Si alloys are currently being considered as strong candidate materials to replace titanium alloys and conventional high-strength aluminum alloys in structural aerospace applications.

The effective utilization of RS Al-Fe-V-Si alloys in structural applications will in many instances be contingent on their ability to be joined to themselves and to dissimilar aluminum and titanium alloys. The unique microstructural characteristics exhibited by RS aluminum alloys preclude the application of many conventional fusion welding processes and methodologies. Major problems in the fusion welding of these aluminum alloys include difficulties in assuring retention of the RS base metal microstructure and the formation of porosity due to a high residual hydrogen content orig-

inating from the aluminum powder or particulates. Preliminary gas tungsten arc welding experiments on an early-generation Al-Fe-V-Si alloy by the authors resulted in unacceptable porosity levels and the formation of coarse, acicular intermetallics.

In recent years, several fusion welding approaches have successfully joined RS Al-Fe-X alloys. Pulsed Nd:YAG laser (Ref. 5) and electron beam welding (Ref. 6) were effectively used for the fusion welding of an RS Al-Fe-Mo alloy characterized by a low hydrogen content. The extremely rapid thermal cycle associated with these processes and low base metal hydrogen content resulted in the formation of fine weld fusion zone (FZ) and heat-affected zone (HAZ) microstructures free of hydrogen-induced porosity. Capacitor discharge welding was used for the fusion welding of an RS Al-Fe-Ce alloy that contained a moderate hydrogen content (Refs. 7 and 8). The simultaneous application of pressure during weld generation and a rapid thermal cycle resulted in a fine, high-strength solidification microstructure free of porosity.

Solid-state joining processes offer an alternate approach to the joining of RS aluminum alloys that are not amenable to joining by fusion welding processes. Diffusion welding and transient liquid phase welding using a silver interlayer have been reported to provide joint efficiencies of up to 70% in Al-Fe-Ce alloys (Ref. 9). Inertia friction welding (IFRW) was also utilized to join Al-Fe-Ce (Ref. 10) and Al-Fe-Mo-V (Ref. 11) alloys which contained high hydrogen. Results showed that the rapid thermal cycle associated with the inertia friction welding process, and the expulsion of

heat- and deformation-affected, plasticized metal out of the weld interface, promoted high-integrity weld zone microstructures and correspondingly high joint efficiencies.

Further studies have demonstrated the feasibility of inertia friction welding RS aluminum alloys to conventional high-strength aluminum alloys (Refs. 10 and 12).

Recent advances in linear friction welding (LFRW) process technology significantly extend the utility of friction welding (FRW) to the joining of nonaxisymmetric parts (Ref. 13). As schematically illustrated in Fig. 2, frictional heating during linear friction welding is provided by the linear translation of two workpiece interfaces through a small amplitude at a suitable frequency vs. their rotational translation during conventional friction welding. Principal variables for this process include the translational amplitude (typically a few mm), the reciprocating frequency, the melt-off displacement, the axial force applied during welding and the final forging force. Although the feasibility of utilizing linear friction welding for the joining of engineering-sized components has recently been demonstrated for several alloys (Ref. 13), relatively little work has been published regarding the metallurgical characterization of linear friction welds and their comparison with conventional friction welds.

The present study was performed to investigate the metallurgical characteristics of inertia friction and linear friction welds in an advanced RS Al-Fe-V-Si alloy, FVS1212, and dissimilar-alloy welds between this alloy and the conventional high-strength aluminum alloy 2024-T351. Specific objectives for the

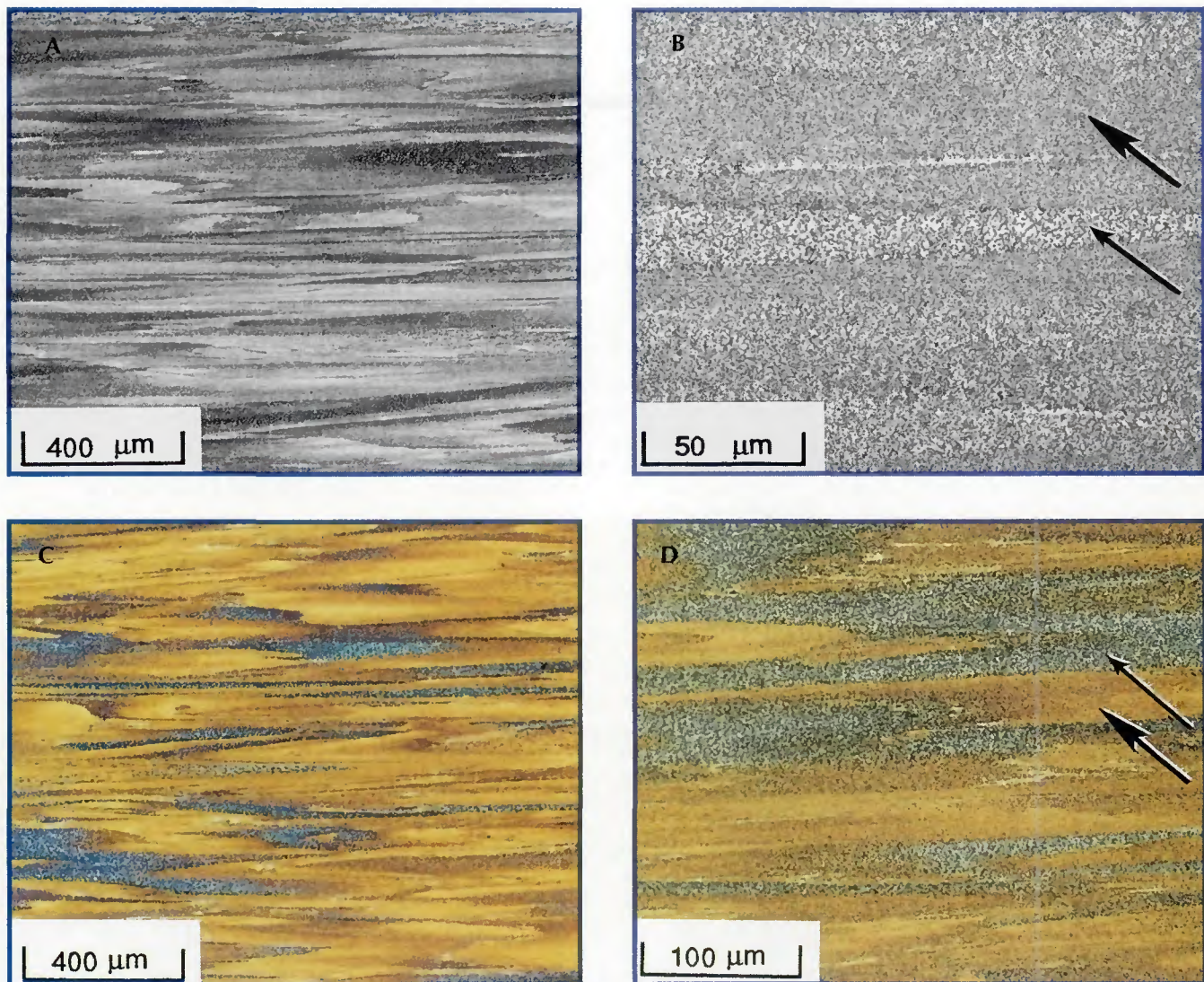


Fig. 3—Light micrographs of as-extruded FVS1212 base metal. Large and small arrows in (B) and (D) indicate regions of fine and coarse dispersoids, respectively.

present work were as follows.

1) Determine the feasibility of producing high-integrity inertia and linear friction welds in FVS1212 and in dissimilar-alloy combination with 2024-T351.

2) Investigate the effects of the welding process on the weld integrity, macro and microstructural characteristics.

3) Establish metallurgical relationships between the weld zone microstructure, mechanical properties and fracture characteristics.

## Experimental Methods

### Materials

The commercially available FVS1212 alloy utilized in this study was produced by Allied-Signal's planar-flow casting process. Following rapid solidification, the ribbons were comminuted into fine

particles, vacuum degassed, hot pressed into billets and finally extruded into a 32-mm (1.26-in.) diameter rod. A 25-mm (1-in.) diameter extrusion of 2024 in a T351 temper condition was utilized in dissimilar-alloy welding studies. Prior to inertia friction welding (IFRW), the rods were sectioned into 50-mm (2-in.) lengths and machined down to a diameter of 22 mm (0.87 in.). Linear friction welds (LFRW) were produced between rods machined down to 25 mm in diameter. Weld faying surfaces were dry machined immediately prior to welding.

### Friction Welding

Inertia friction welds were produced using an MTI Model 120 inertia friction welding system. Welding parameters were selected based on previous inertia friction welding studies of dispersion-strengthened aluminum alloys (Refs. 10

and 11). Similar-alloy welds in FVS1212 and dissimilar-alloy welds between FVS1212 and 2024-T351 exhibiting two levels of axial displacement were produced by varying the axial force. Similar-alloy and dissimilar-alloy linear friction welds were produced using a machine located at The Welding Institute in Cambridge, England. Welding parameters utilized for each process are shown in Table 1. It is important to note that welds were produced to demonstrate feasibility of the process, and not to fully optimize the weld structure and mechanical properties.

### Weld Characterization

After welding, the weld axial displacement and flash uniformity were visually evaluated. Representative welds were sectioned axially in a direction parallel to the displacement motion,

**Table 1—Welding Parameters for the Alloy/Process Combinations**

Welding Process/Parameter	Similar-Alloy Welds FVS1212	Dissimilar-Alloy Welds FVS1212/2024-T351
Inertia friction welds		
Moment of inertia	0.12 kg·m <sup>2</sup> (3.94 lbm·ft <sup>2</sup> )	0.12 kg·m <sup>2</sup> (3.94 lbm·ft <sup>2</sup> )
Rotational speed	524 rad/s	367 rad/s
Axial force	55.8, 83.7 kN (12.4, 18.6 klf)	83.7, 139.5 kN (18.6, 31.0 klf)
Linear friction welds		
Friction force	30.0 kN (6.7 klf)	30.0 kN (6.7 klf)
Forge force	50.0 kN (11.1 klf)	50.0 kN (11.1 klf)
Frequency	50 Hz	50 Hz
Translation amplitude	2 mm (0.079 in.)	2 mm (0.079 in.)
Melt-off	4 mm (0.157 in.)	4 mm (0.157 in.)

mounted in epoxy, mechanically ground down with 600-grit SiC paper, rough polished with 3-micron diamond compound and 0.3-micron alumina and final polished using a colloidal silica suspension. Following defect analysis of the as-polished specimen surfaces using light microscopy, microstructural features were revealed by etching with Keller's reagent.

Alternate specimen halves were carefully sectioned longitudinally at the axial centerline into thin slices 0.3-mm (0.01-

in.) in thickness and mechanically thinned down to 0.125 mm (0.005 in.). Disks 3 mm (0.12 in.) in diameter were punched from the foils in the unaffected base metal and from representative regions in the weld heat- and-deformation affected zones (HDZ) and electrojet polished in one part nitric acid and three parts methanol at -30 °C (-22°F). Thin foils were examined in a JEOL 200CX analytical-electron microscope equipped with a Tracor-Northern TN-2000 energy dispersive x-ray analysis (EDS) system.

Knoop microhardness testing (150-g load) was performed across the weld region at the axial centerline and the outer periphery for correlation with microstructural characteristics. Transverse-weld-oriented tensile test specimens (gauge section: 25 mm length X 4.5 mm width X 1.5 mm thickness/ 1 X 0.18 X 0.06 in.) were sectioned from the center and outer periphery of each weld type and tested as per ASTM E8-87 at an extension rate of 0.25 mm/min. Also, three-point guided bend testing was performed on axial half sections to reveal the fracture characteristics. Following mechanical testing, fracture surfaces were characterized using light and scanning electron microscopy (SEM).

## Results and Discussion

### Base Metal Characterization

The microstructure of the FVS1212 base metal oriented parallel to the extrusion direction is shown in black-and-white contrast in Fig. 3A, B and in color contrast in Fig. 3C, D. Boundaries between the individual particles are clearly

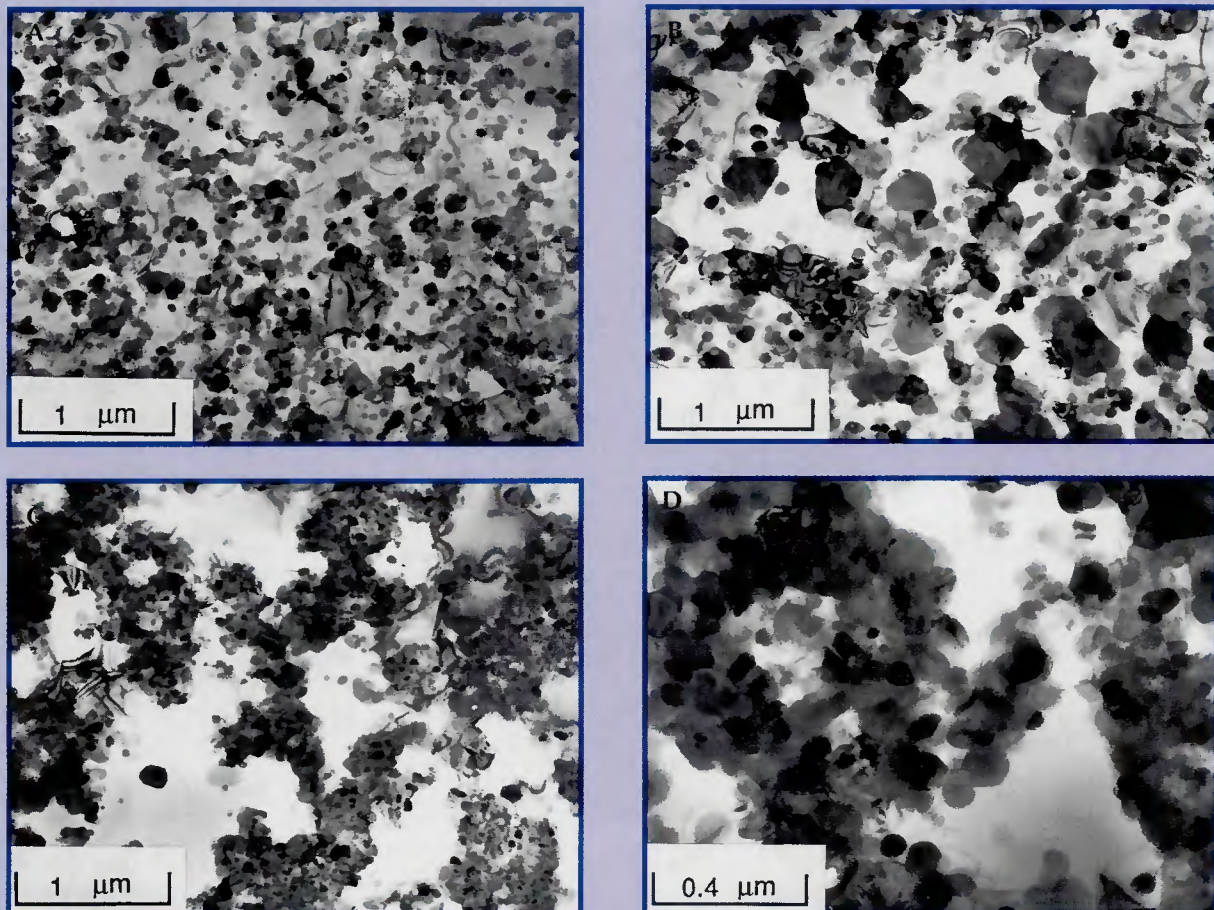


Fig. 4 TEM bright-field micrographs of FVS1212 extruded base metal. A — Uniform distribution of fine dispersoids; B — mixture of fine and coarse dispersoids; C, D — clusters of fine dispersoids along alpha grain boundaries.

observable at low magnification. Regions of dark contrast in Fig. 3A, which contained coarser dispersoids, conversely exhibited light contrast in Fig. 3B at increased magnification. The white alpha aluminum matrix between the dispersoids was readily observable at high magnification. Regions of light contrast in Fig. 3A, which contained extremely fine dispersoids, actually appeared dark at higher magnification in Fig. 3B. Occasionally, narrow white bands devoid of dispersoids were observed.

Color contrast light micrographs more clearly revealed microstructural details of the base metal (Fig. 3C and D). Regions of fine dispersoids exhibited a yellow contrast (large arrow in Fig. 3D), while regions of coarser dispersoids exhibited a blue contrast (small arrow in Fig. 3D). Regions containing mixtures of both coarse and fine dispersoids exhibited a dark brown contrast. The microstructural variations within a single particle (as revealed by different colors) originated from differences in the cooling rate across the original ribbon, with the side contacting the quenching wheel experiencing appreciably higher cool-

ing rates than the opposite free surface side. Higher cooling rates correspondingly promoted a finer as-solidified microstructure and ultimately a finer as-processed dispersoid/grain structure.

Transmission electron microscope (TEM) observation further delineated microstructural characteristics of the FVS1212 base metal, as shown in Fig. 4. Consistent with light microscopy observations, low-magnification TEM bright-field micrographs revealed distinct boundaries between the original ribbon particles and differences in the size and distribution of the dispersoids throughout the microstructure. TEM examination at an increased magnification showed three different regions in regard to the dispersoid size and distribution: 1) fine dispersoids, 2) a mixture of fine and coarse dispersoids and 3) clusters of fine dispersoids. Figure 4A shows a region containing nearly spherical, fine-sized dispersoids ranging in diameter from about 75 to 100 nm. Another representative region showed a bimodal distribution of dispersoids consisting of fine dispersoids ranging from 50 to 100 nm in diameter and coarser dispersoids up

to 400 nm in diameter — Fig. 4B. Alpha aluminum grains in these regions were equiaxed and ranged in diameter from 0.5 to 1 micron. TEM analysis of the regions that exhibited coarse dispersoids and a high proportion of alpha phase at low magnification (region indicated by small arrow in Fig. 3B) showed clusters of fine dispersoids (50 to 100 nm in diameter) located at alpha grain boundaries (Fig. 4C and D). The population density of dispersoids in this region was generally lower than the regions of uniform, fine dispersoid distribution (Fig. 4A), and the alpha grain size was also coarser, up to about 1.5 microns in diameter. It is suggested that the formation of these structures may be associated with slowly cooled regions on the free surface side of the PFC ribbons. Occasionally, dispersoid-free bands shown in Fig. 3B were observed, which may have originated from nonhomogenous deformation during extrusion. Previous studies on these alloys (Refs. 3 and 4) indicated the dispersoids to be uniquely  $\text{Al}_{13}(\text{Fe}, \text{V})_3 \text{Si}$  type. Acicular dispersoids observed in previous studies of an RS Al-Fe-Mo-V alloy (Ref. 11) were not ob-

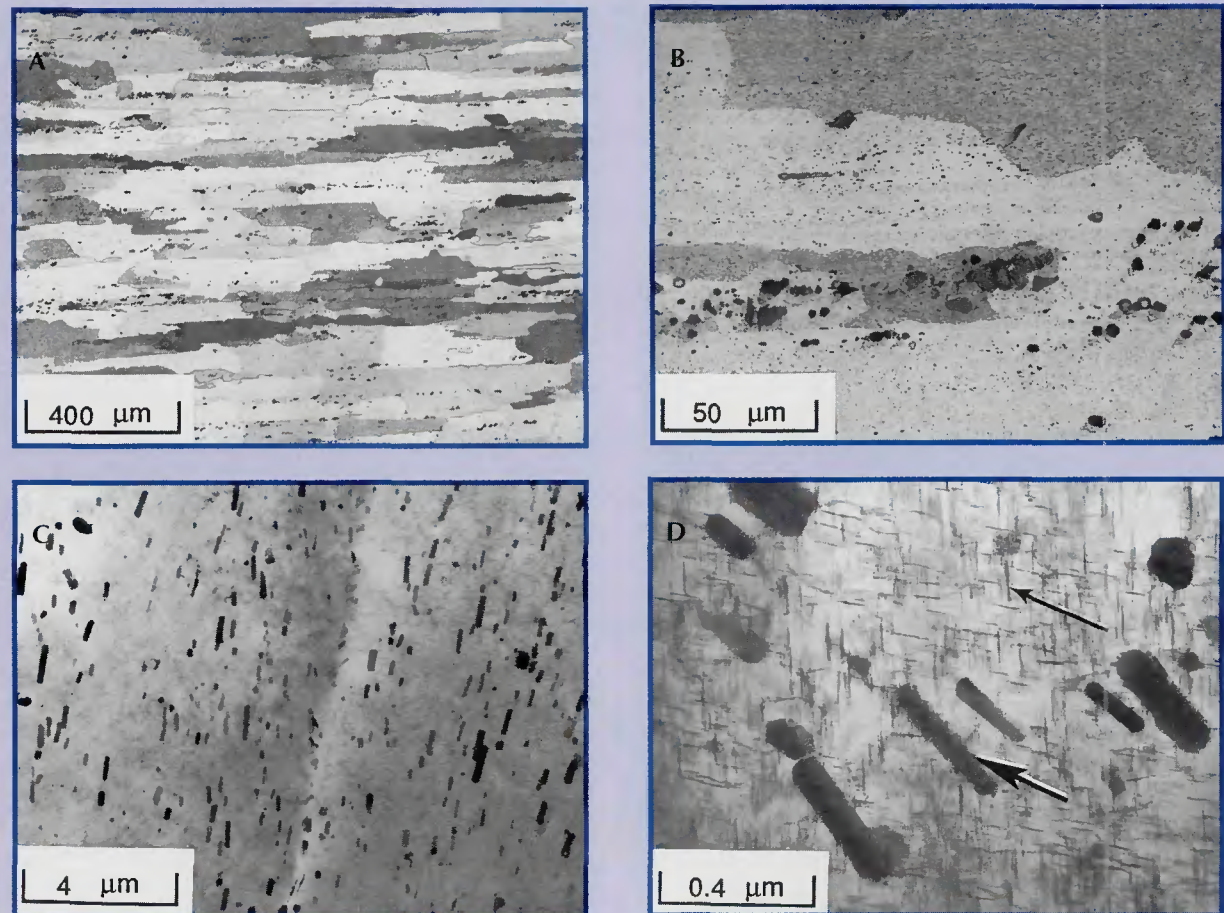
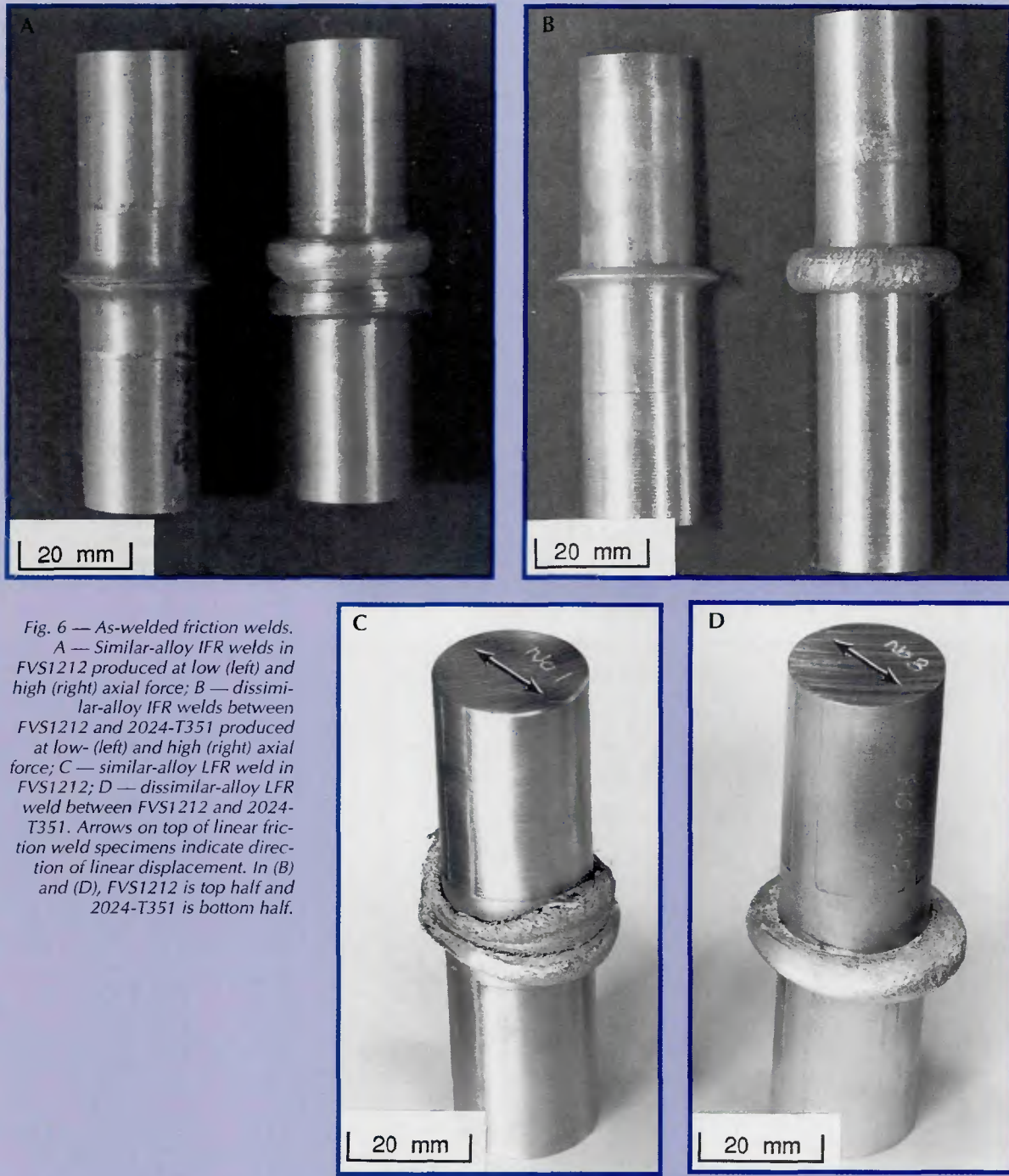


Fig. 5 — Micrographs of 2024-T351 base metal. A, B — Light and C, D — TEM bright-field. Large and small arrows in (D) indicate  $\text{Al}_{20}\text{Cu}_2\text{-Mn}_3$  dispersoids and  $S'$  ( $\text{Al}_2\text{CuMg}$ ) precipitates, respectively.



*Fig. 6 — As-welded friction welds.*  
A — Similar-alloy IFR welds in FVS1212 produced at low (left) and high (right) axial force; B — dissimilar-alloy IFR welds between FVS1212 and 2024-T351 produced at low- (left) and high (right) axial force; C — similar-alloy LFR weld in FVS1212; D — dissimilar-alloy LFR weld between FVS1212 and 2024-T351. Arrows on top of linear friction weld specimens indicate direction of linear displacement. In (B) and (D), FVS1212 is top half and 2024-T351 is bottom half.

served. This result confirms the previously observed influence of vanadium in stabilizing the cubic  $\text{Al}_{13}(\text{Fe},\text{V})_3\text{Si}$  over the hexagonal  $\text{Al}_8\text{Fe}_2\text{Si}$  or monoclinic  $\text{Al}_3\text{Fe}$  phases (Ref. 3).

Figure 5A–B shows light micrographs of the 2024-T351 base metal oriented parallel to the extrusion direction. The microstructure exhibited light and dark contrast depending on the orientation of alpha grains or subgrains — Fig. 5A. Observation at a higher magnification

showed agglomerations of various dispersoids and precipitates at grain boundaries and fine particles within the grains — Fig. 5B. TEM bright-field imaging revealed columnar intermetallic particles and fine, intragranular precipitates (Fig. 5C and D). Based on the morphology of these particles (Ref. 14) and EDS analysis, the small, lath-type precipitates were identified as precursor S' ( $\text{Al}_2\text{CuMg}$ ) particles and the coarse, columnar particles were identified as  $\text{Al}_{20}\text{Cu}_2\text{Mn}_3$  disper-

soids. Despite extreme care, the coarse, grain boundary dispersoid particles underwent preferential attack during electropolishing and could not be effectively characterized.

## Weld Zone Characterization

### Macroscopic Analysis

The as-welded inertia friction (IFR) and linear (LFR) friction welds are shown

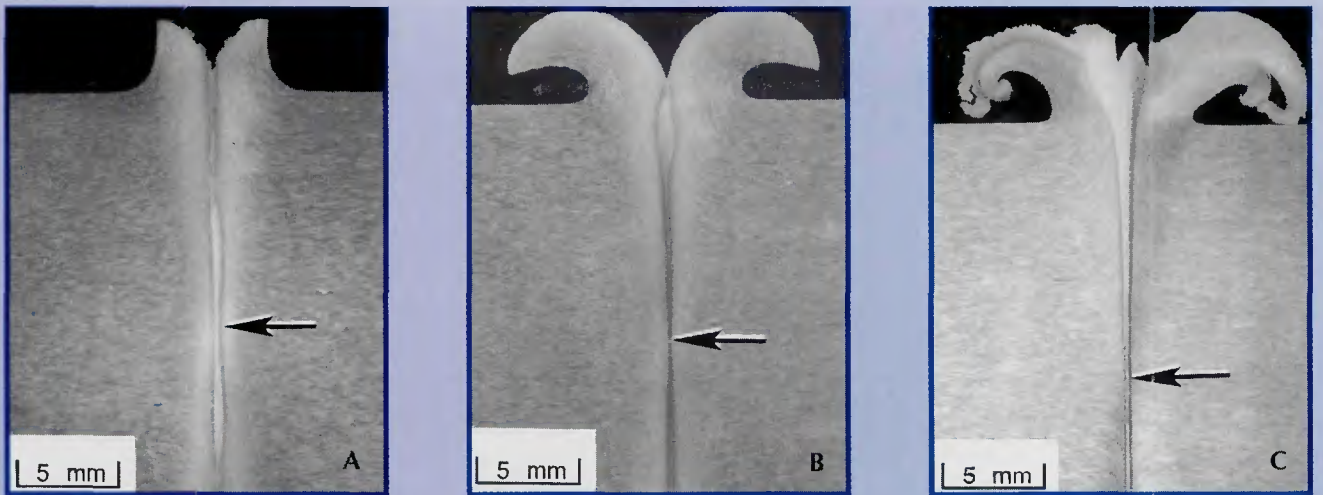


Fig. 7 — Macrographs of the similar alloy welds in FVS1212. A — Inertia friction weld produced with low axial force; B — inertia friction weld produced with high axial force; C — linear friction weld. Arrows indicate axial center line.

in Fig. 6. Visual examination of the similar-alloy IFR welds indicated the presence of smooth, symmetrically uniform flash around the entire weld circumference, with the quantity of flash increasing with an increase in axial force. The axial displacement likewise increased with an increase in axial force, from 4.5 to 8.9 mm (0.18 to 0.35 in.). Consistent with the appreciably lower elevated-temperature strength of 2024-T351 relative to FVS1212, dissimilar-alloy IFR welds exhibited preferential flash formation in 2024-T351 vs. the FVS1212. As in the similar alloy IFR welds, an increase in axial force promoted a greater extent of flash and higher axial displacement (7.1 vs. 2.4 mm/ 0.28 vs. 0.09 in.).

Similar-alloy LFR welds exhibited flash formation around the entire circumference, but principally in the di-

rection of linear displacement. Dissimilar-alloy LFR welds exhibited flash only in 2024-T351, which was circumferentially more uniform than observed in the similar-alloy LFR welds. The axial displacements measured for the similar-alloy and dissimilar-alloy linear friction welds were 6.5 and 5.2 mm (0.26 and 0.20 in.), respectively, and therefore were intermediate between those values measured for the inertia friction welds. Note that these displacements were greater than the preset 4 mm (0.16 in.) melt-off displacement due to the additional upset experienced during application of the forge force.

Examination of the as-polished surfaces of each specimen revealed no evidence of defects except at the very outer periphery of the dissimilar-alloy LFR weld.

Macrographs of the axially sectioned weld specimens for different alloy/parameter combinations are shown in Figs. 7 and 8. Similar-alloy IFR welds exhibited hourglass-shaped heat- and deformation zones, which decreased in width with an increase in axial force — Fig. 7A and B). The center of the HDZs (referred to hereafter as the inner HDZ) exhibited featureless regions of light and/or dark contrast. In the low axial force IFR weld, a light-contrast center was surrounded by a region exhibiting dark contrast, while in the high axial force IFR weld, only a region of dark contrast was apparent. The width of the inner HDZ remained relatively constant across the low axial force IFR weld, and gradually decreased in width toward the axial centerline in the high axial force IFR weld. Macrostructural features of the similar-

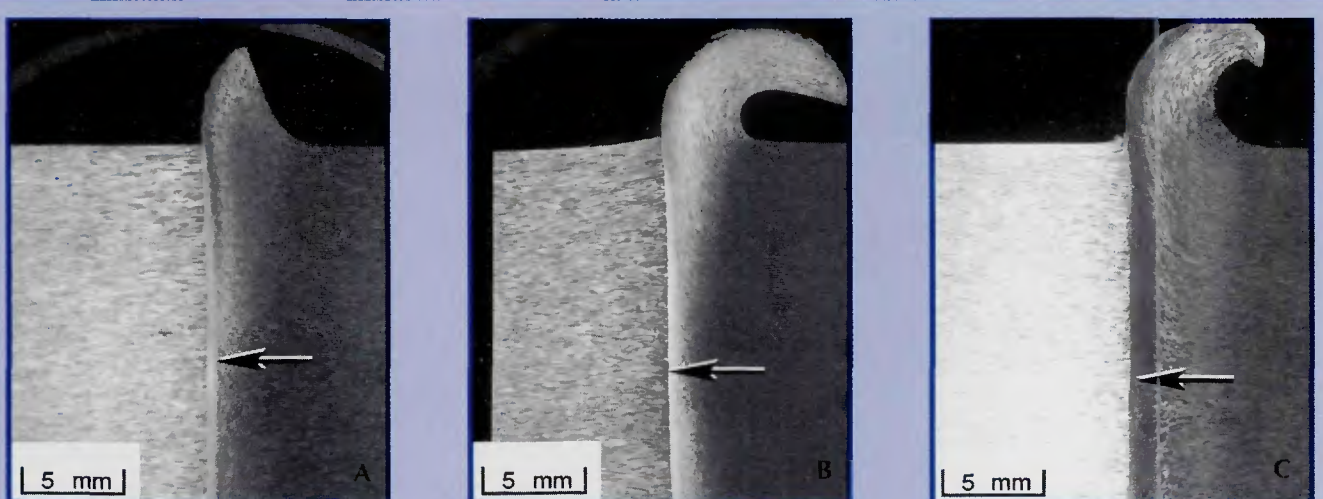


Fig. 8 — Macrographs of the dissimilar-alloy welds between FVS1212 and 2024-T351. A — Inertia friction weld produced with low axial force; B — inertia friction weld produced with high axial force; C — linear friction weld. Arrows indicate axial centerline.

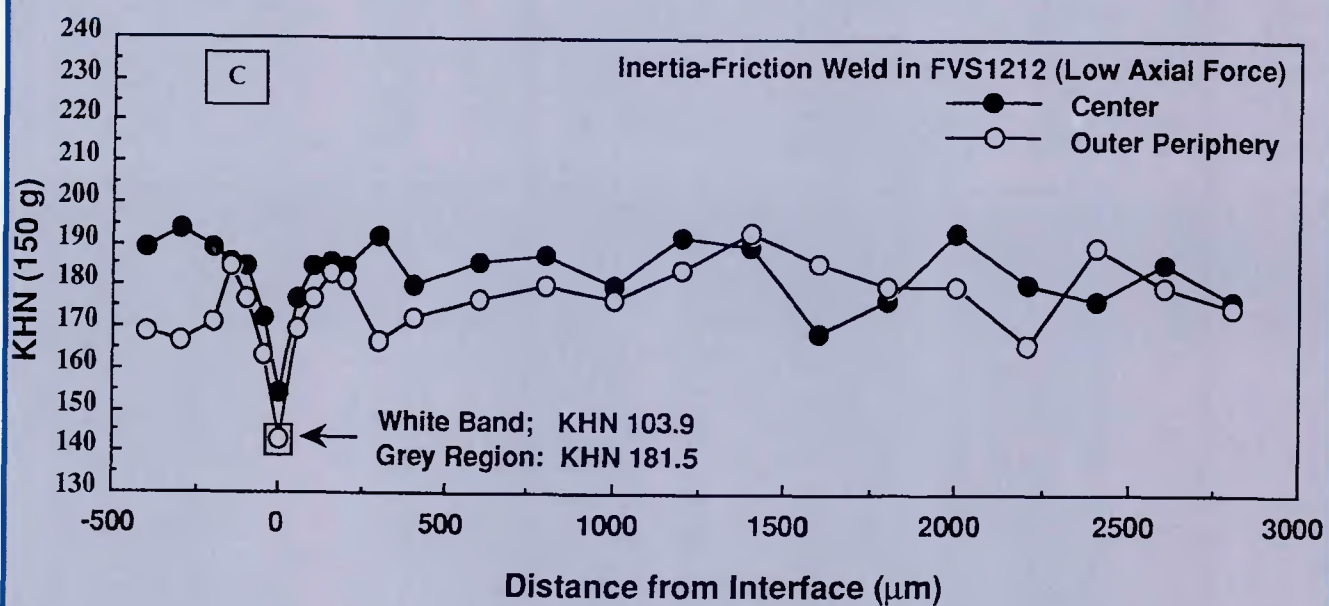
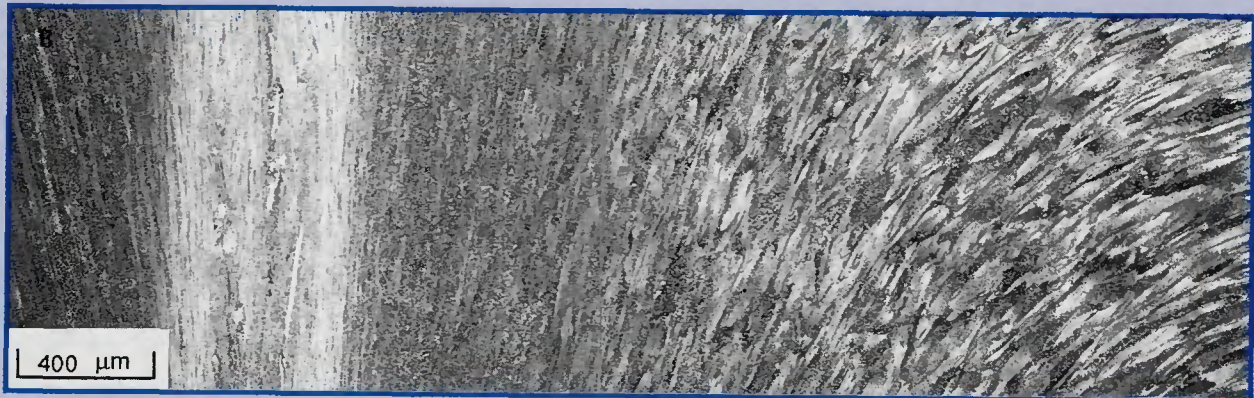
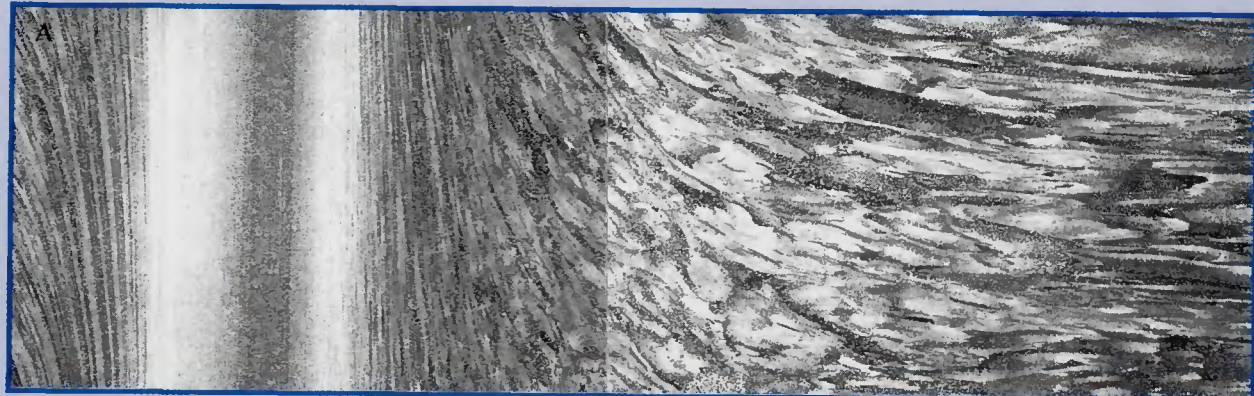


Fig. 9 — Light micrographs of an inertia friction weld produced in FVS1212 using low axial force. A — Center; B — outer periphery; C — corresponding KHN traverses.

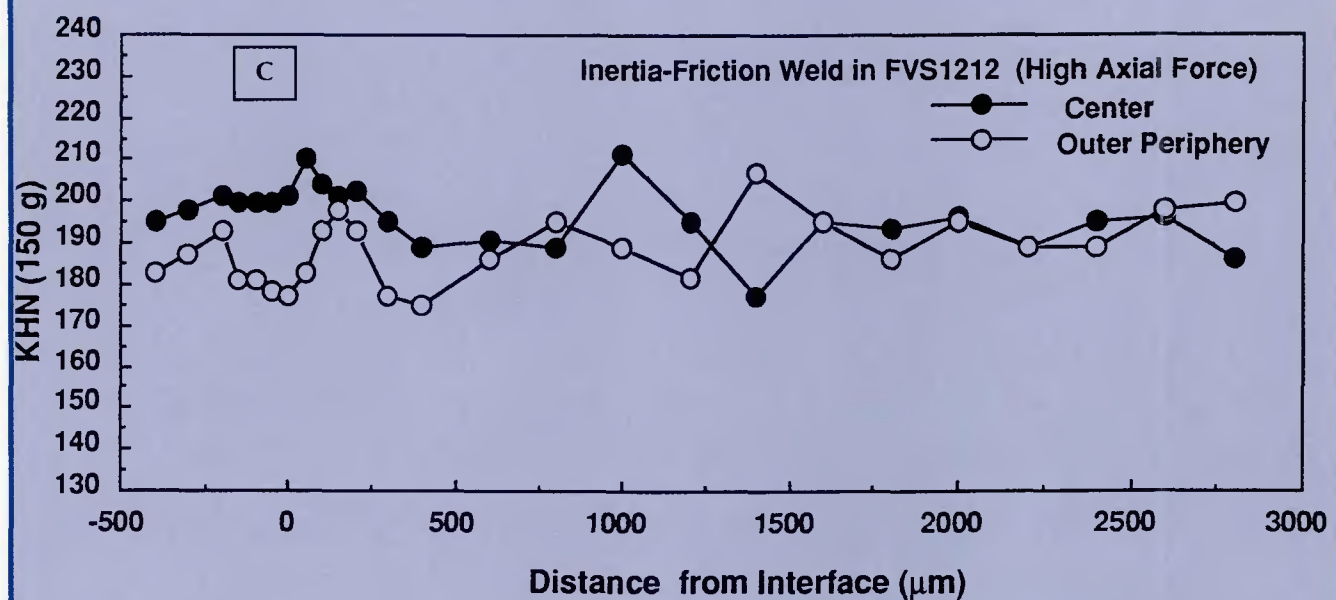
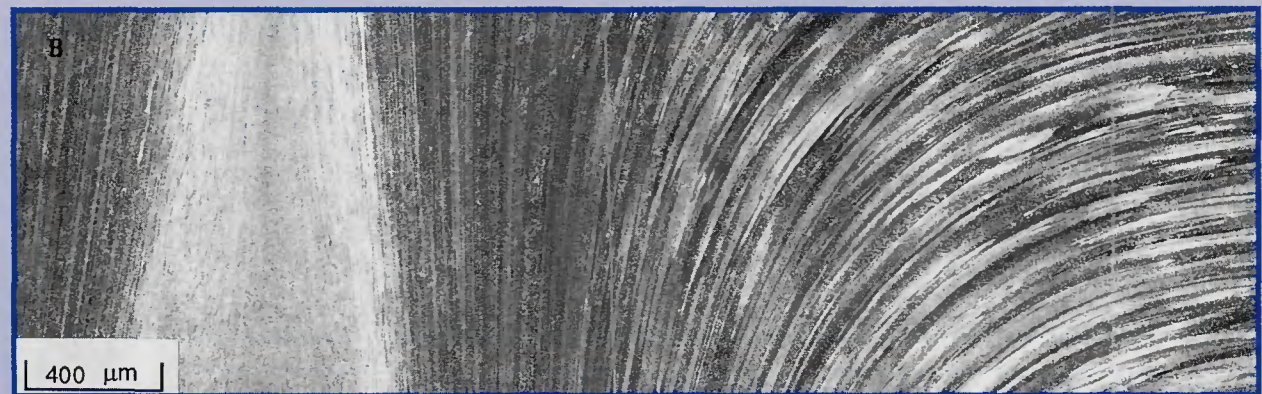


Fig. 10 — Light micrographs of an inertia friction weld produced in FVS1212 using high axial force. A — center; B — outer periphery regions; C — corresponding KHN traverses.

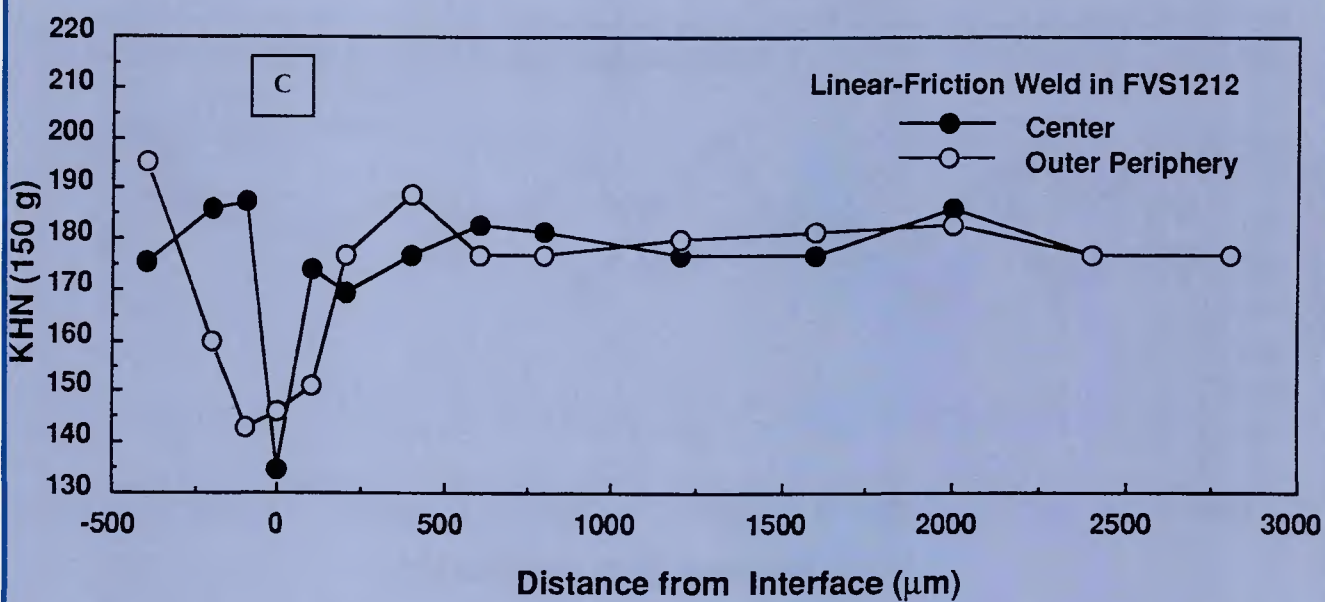
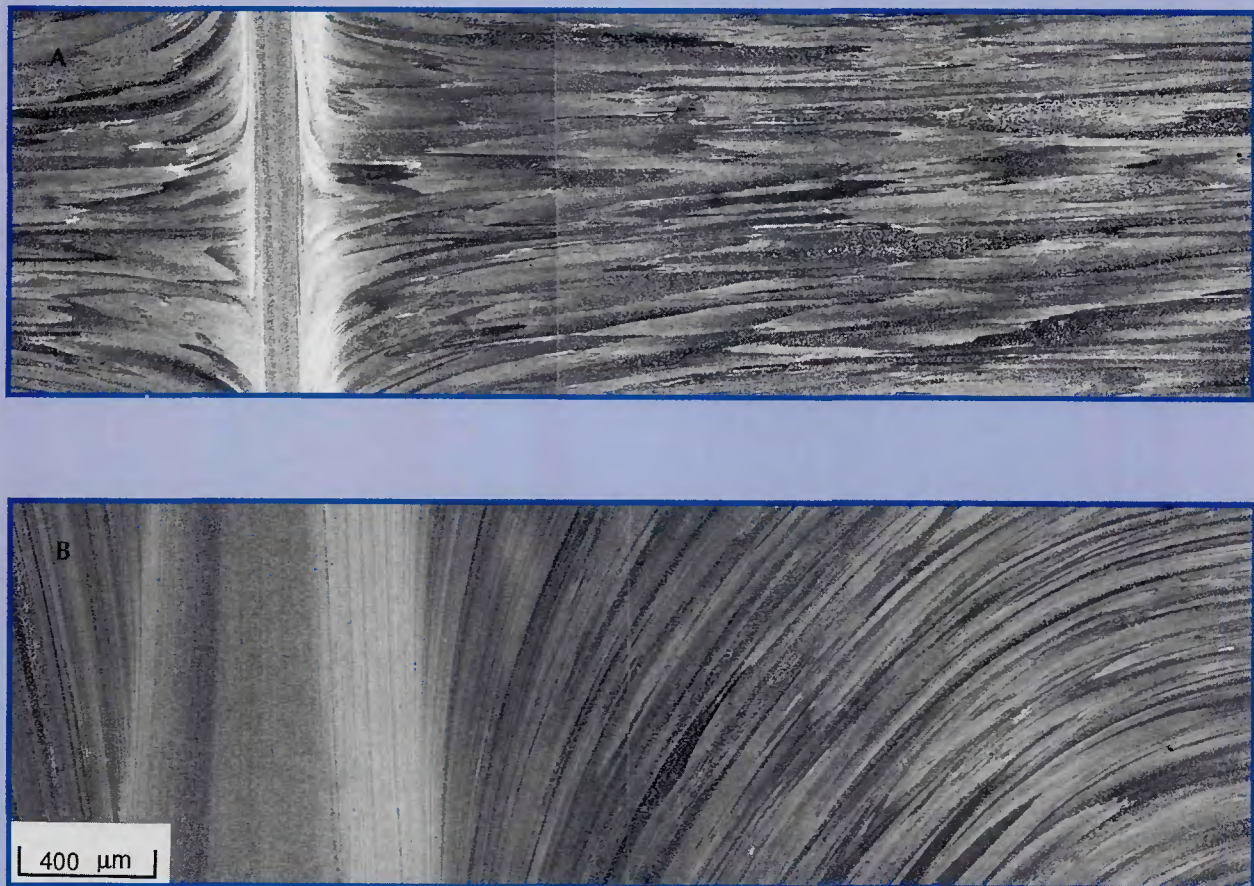
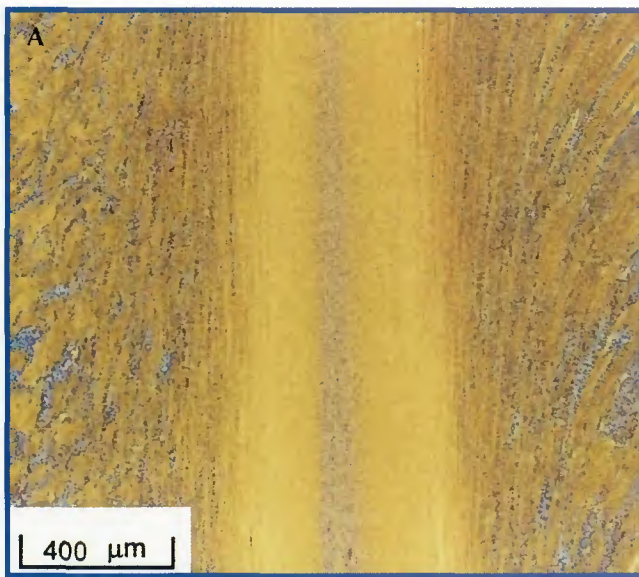


Fig. 11 — Light micrographs of a linear friction weld produced in FVS1212. A — Center; B — outer periphery; C — corresponding KHN traverses.



*Fig. 12 — Light micrographs of the interface regions at the axial center lines of friction welds in FVS1212. A — Inertia friction weld produced using low axial force; B — linear friction weld.*

alloy LFR welds showed similar features to those of the IFR welds — Fig. 7C. Interestingly, the inner HDZ was comprised of adjacent regions of light contrast (left side) and dark contrast (right side), which gradually decreased in total width from the outer periphery to the axial centerline.

The dissimilar-alloy IFR welds exhibited an hourglass-shaped HDZ only in the 2024-T351 — Fig. 8A and B. The effect of the axial force was similar to the similar-alloy IFR welds. The macrostructure of the dissimilar-alloy LFR welds showed similar features to those of the dissimilar-alloy IFR welds — Fig. 8C. The width of the outer HDZ in the dissimilar-alloy LFR weld was noticeably wider than that of the dissimilar-alloy IFR welds.

#### Light Microscopy Analysis

Figures 9–11 and 13–14 show microstructures and corresponding hardness traverses from the unaffected base metal to the center of the weld HDZ at the axial centerline and outer periphery for each alloy/process combination.

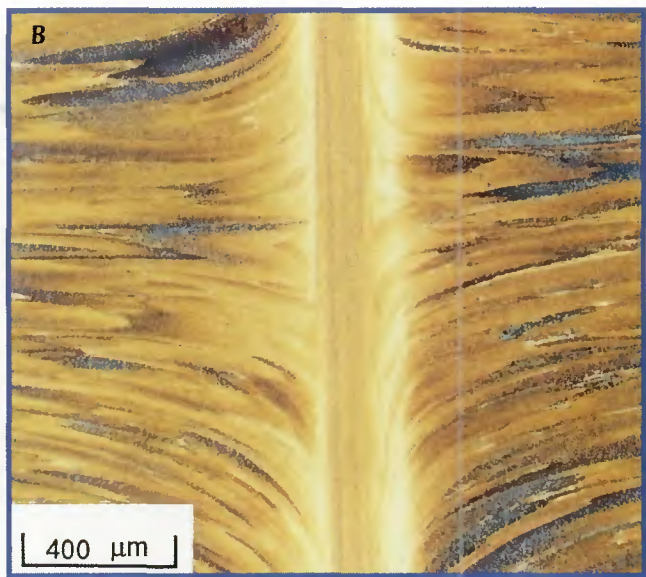
#### Similar-Alloy Welds

For the similar-alloy IFR (Figs. 9 and 10) and LFR (Fig. 11) welds, the base metal microstructure showed a continuous reorientation from parallel to perpendicular to the original base metal extrusion direction. Nearer to the center of the weld HDZ, the reoriented microstructure became increasingly “flattened” due to high axial compressive stresses. Comparing Figs. 9, 10 and 11, the width of the inner HDZ was greater

for the IFR welds produced at both the high- and low axial force as compared to the LFR weld.

In the inner HDZ of the low axial force weld, variations, that originally existed in the base metal microstructure, were less apparent due to severe mechanical mixing and homogenization. As shown, the inner HDZ was comprised of a gray central region and a white outer region (note that the contrast of these regions are actually the reverse of those observed at low magnification). The color light micrograph in Fig. 12 effectively reveals the microstructural changes near the weld interface region. In the IFR welds, the base metal microstructure became increasingly homogeneous and yellow in color at the boundary region between the inner HDZ and outer HDZ, showing an absence of the blue, coarse-sized dispersoid regions — Fig. 12A. The center region of the homogeneous inner HDZ, which showed gray contrast in black-and-white micrographs, appeared bluish-yellow or brown, implying some coarsening in the dispersoid and grain sizes. The inner HDZ at the outer periphery region of the low axial force IFR weld exhibited a gray contrast central region and neighboring light contrast region similar to the axial center. However, narrow, white bands and adjacent dark regions were also observed in the inner HDZ at the interface — Fig. 9B. Examination at increased magnification indicated a very low dispersoid density in the light regions and a higher dispersoid density in the adjacent dark regions vs. the surrounding inner HDZ.

Figure 10A–B shows microstructure traverses across the high axial force IFR



weld in FVS1212. In the inner HDZ, the region of gray contrast was barely observable. The higher compressive stress expelled the homogenized and coarsened microstructure to the outer periphery, leaving only the fine-textured structure as observed in the white-contrast region in the low axial force weld. The outer periphery region of the weld exhibited an appreciably wider HDZ, which appeared comparable to the center of the low axial force weld. Dispersoid-lean bands were not observed in the high axial force weld. The absence of these structures in high axial force welds was attributed to the increased expulsion of the softened metal from the weld interface.

Figure 11A and B shows microstructure traverses across the LFR weld in FVS1212. Compared with the IFR welds, the inner HDZ was macroscopically homogeneous but comprised of several narrow, gray and white contrast layers. The transition from the inner HDZ to the outer HDZ was more abrupt than in the IFR welds. The outer periphery region exhibited an asymmetric inner HDZ, with one side showing white contrast and the other side showing gray contrast. The color light micrograph of the LFR weld (Fig. 12B) showed light-yellow color at the boundary region with the inner HDZ and streaks of brown or bluish-yellow at the center of the inner HDZ, indicating dispersoid coarsening in this region.

#### Dissimilar-Alloy Welds

For the dissimilar-alloy IFR welds (Fig. 13) and LFR weld (Fig. 14), microstructural changes and reorientation of the

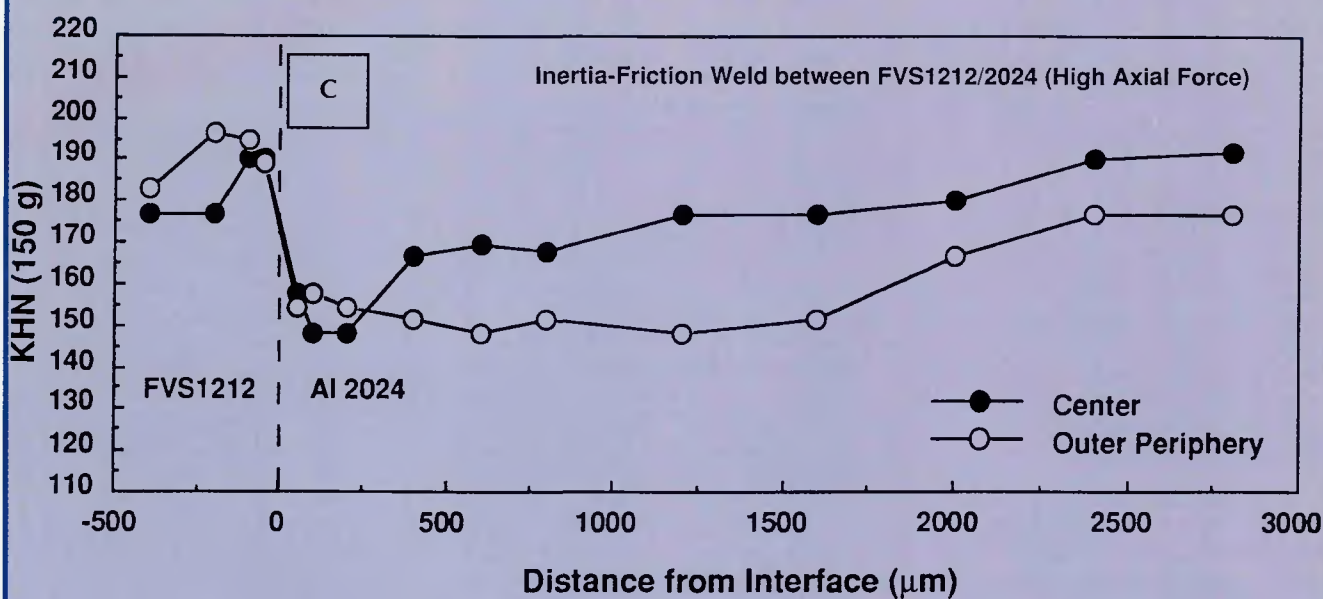
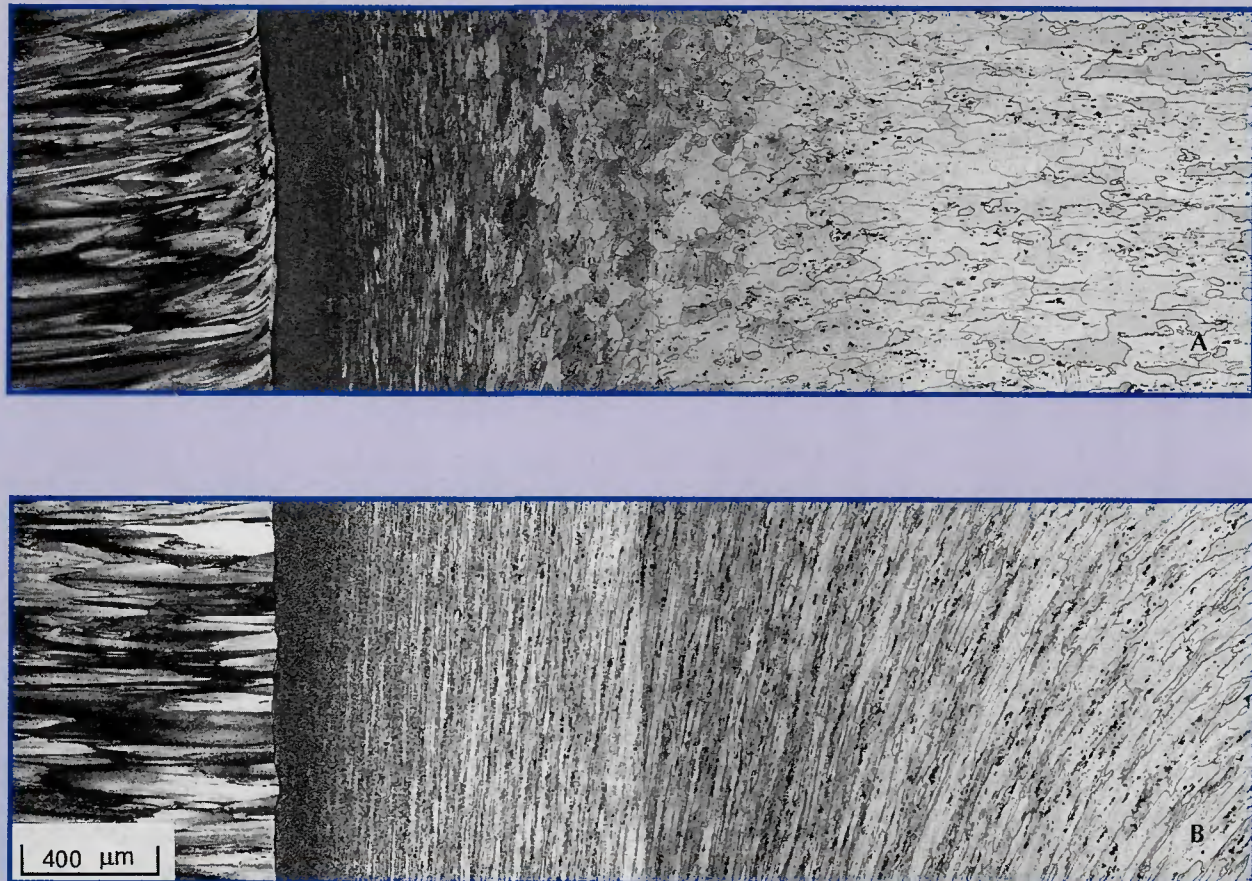


Fig. 13 — Light micrographs of an inertia friction weld between FVS1212 and 2024-T351 produced using high axial force. A — Center; B — outer periphery; C — corresponding KHN traverses.

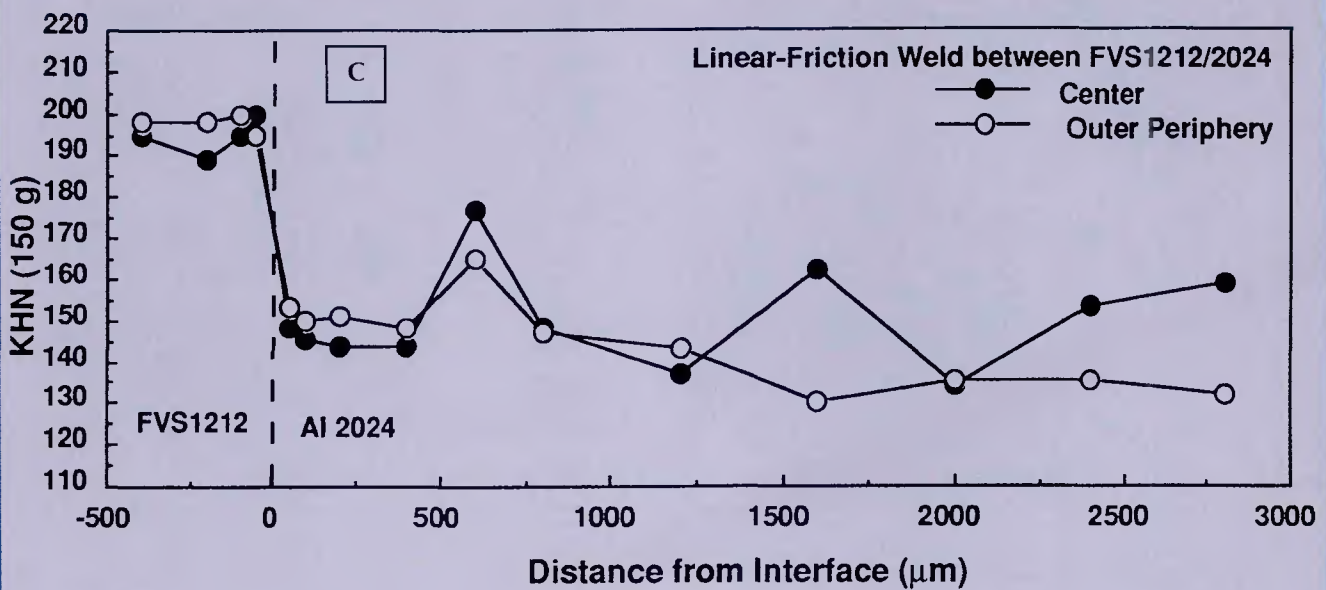
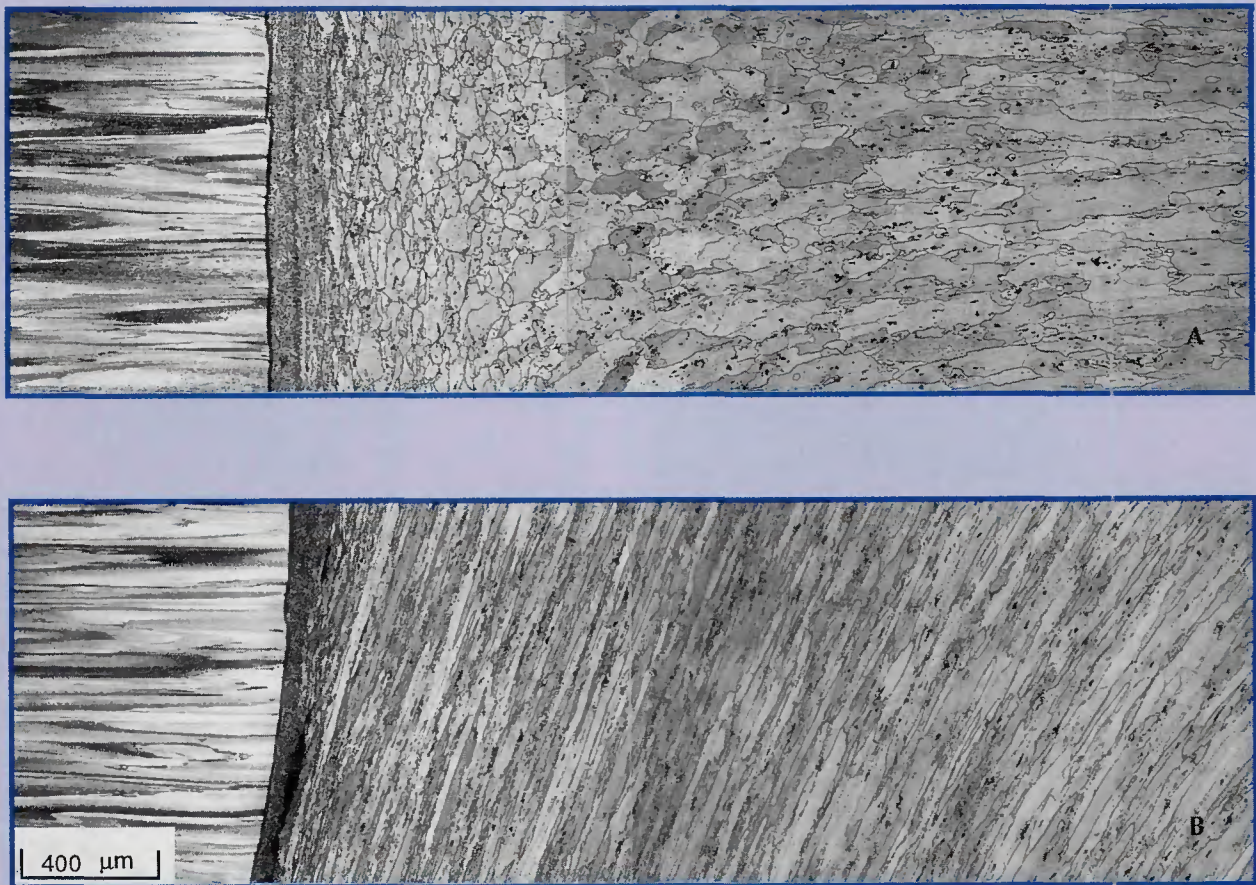


Fig. 14 — Light micrographs of a linear friction weld between FVS1212 and 2024-T351. A — Center; B — outer periphery regions; C — corresponding KHN traverses.

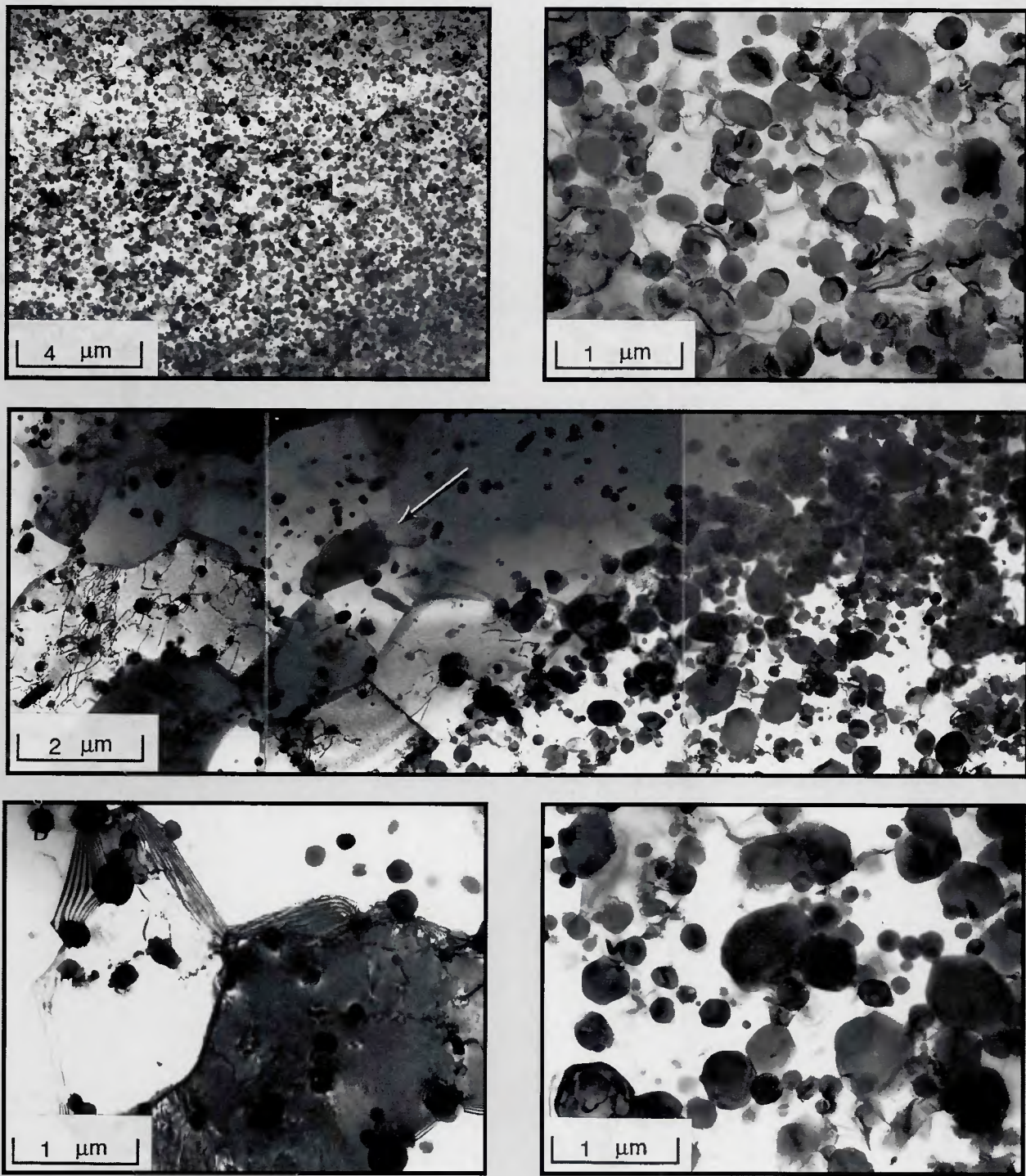


Fig. 15 — TEM bright-field micrographs of IFR welds produced in FVS1212 using low axial force. A, B — Center of HDZ at axial centerline; C-E — center of HDZ at outer periphery. Arrow in (C) is parallel to weld interface.

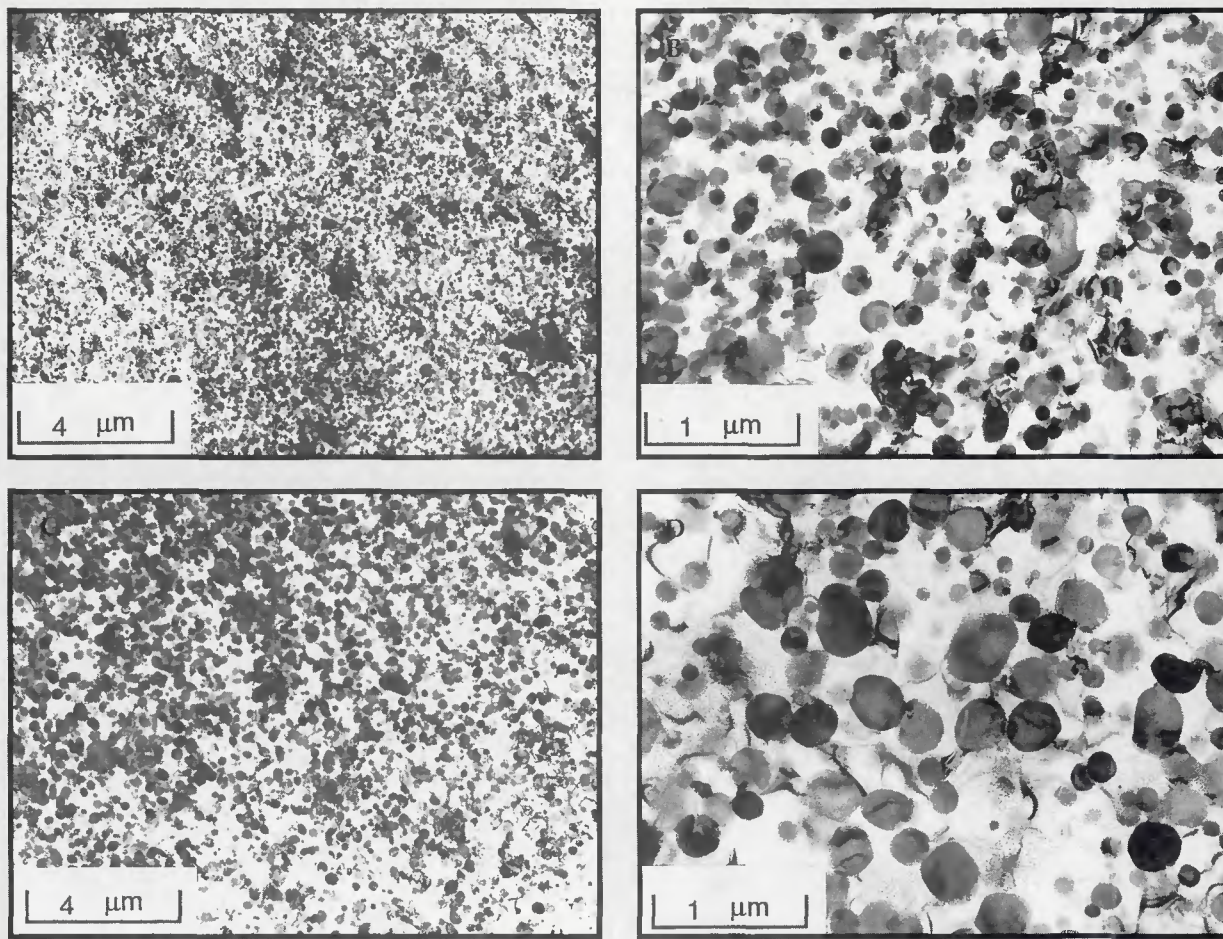


Fig. 16 — TEM bright-field micrographs of IFR welds produced in FVS1212 using high axial force. A, B — Center of HDZ at axial centerline; C, D — center of HDZ at outer periphery.

base metal structure were observed only in the 2024-T351. Outer HDZs at the axial centerline exhibited elongated alpha grains in the base metal, which gradually changed to near-equiaxed grains, and then to a severely laminated structure and finally to a featureless (dark contrast) microstructure within the inner HDZ. At the outer periphery of each weld, elongated alpha grains gradually became reoriented and flattened, with a similar dark contrast microstructure at the inner HDZ. The width of the inner HDZ was greater in the IFR welds than in the LFR weld. Contrary to the similar alloy welds, the width of the inner HDZ at the outer periphery was narrower than at the center for both the IFR and LFR welds.

#### TEM Analysis

##### Similar-Alloy Welds

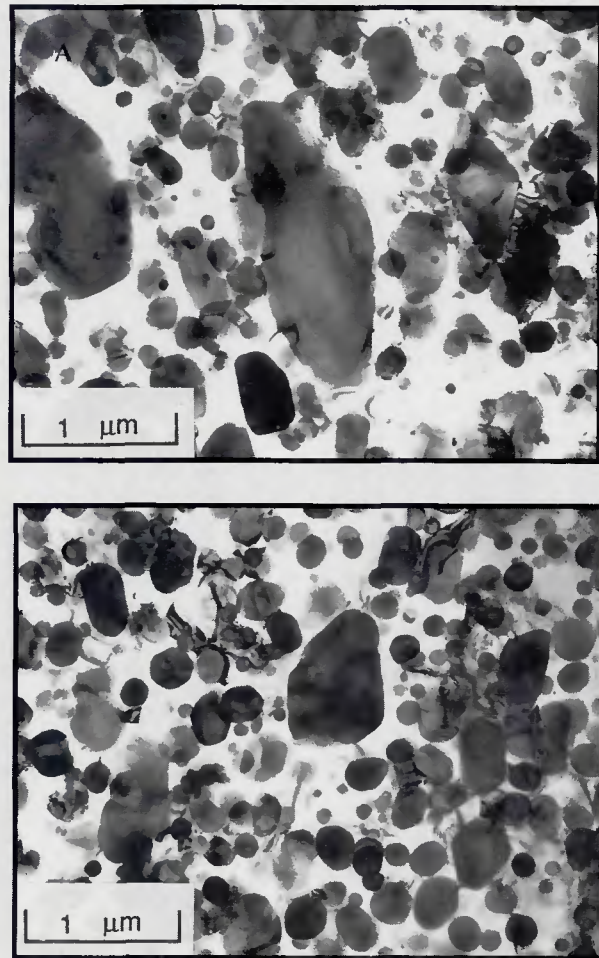
TEM bright-field analysis of the inner HDZ at the axial centerline in the similar-alloy IFR weld produced with low axial force (Fig. 15A and B) showed a

relatively homogenous distribution of dispersoids ranging in size from about 75 to 500 nm. The clusters of fine dispersoids shown in Fig. 4C and D were not observed in this region, indicating their complete break-up and dispersion. The dispersoid sizes and size distribution in this region were generally comparable to those observed in the unaffected base metal, showing only a marginal increase in the range of dispersoid sizes. While the previous TEM analysis of inertia friction welds in Al-Fe-Mo-V alloys (Ref. 11) showed the cleavage-type fracture of relatively coarse dispersoids (up to two microns in diameter) in the inner HDZ, no evidence of dispersoid fracture was observed in this study. The inner HDZ of the low axial force weld adjacent to the homogenized center region exhibited alternating regions of light- and dark-appearing contrast at lower magnification. These observations were attributed to variations in the dispersoid population density and distribution, with dark contrast for regions of a higher dispersoid population density and light contrast for regions of a lower

population density. Regions containing clusters of fine dispersoids were also observed to exhibit light contrast. These differences in dispersoid size and distribution were associated with variations in the original base metal microstructure which had been "flattened" but not completely homogenized. The alpha aluminum grains in inner HDZ regions showed a similar morphology and size to those observed in the base metal, being nearly equiaxed and ranging in diameter from about 0.25 to 1.0 microns. Considering the equiaxed nature and the size of the grains, and their low-dislocation density, it is suggested that the grains were dynamically-recrystallized on weld cooling and that the growth was limited by the high volume fraction of dispersoids.

TEM bright-field micrographs in Fig. 15C-E show a region containing dispersoid-lean bands at the outer periphery of the IFR welds produced using low axial force (white-appearing bands in Fig. 9B). In addition to a low-dispersoid population density, this region contained coarser alpha grains up to several

*Fig. 17 — TEM bright-field micrographs of LFR welds produced in FVS1212. A — Center of HDZ at axial centerline; B — adjacent layered region; C — center of HDZ at outer periphery.*



microns in diameter with a slightly elongated morphology. The low-dispersoid density in this region allowed limited alpha grain growth. One explanation for the occurrence of this microstructure may be localized melting of the alpha phase at the weld interface, which, if present, would occur at the outer periphery due to the higher rotational velocities and peak temperatures. However, analysis of the regions indicated no evidence of a resolidified microstructure. Alternatively, the microstructure could result from localized, nonuniform deformation in the HDZ. High tensile compressive stresses in combination with simultaneous shear stresses in this region may locally extrude soft alpha aluminum from the original base metal microstructure, resulting in dispersoidlean regions. The presence of adjacent, dark-contrast regions, which contained a high population density of dispersoids (Fig. 9B), may be explained by such nonuniform deformation.

TEM bright-field micrographs in Fig. 16A and B show the inner HDZ at the axial centerline of the IFR weld pro-

duced using high axial force. Considerable homogenization was indicated by the uniform distribution of a wide range of dispersoid sizes. The adjacent inner HDZ exhibited regions of alternating dark- and light-appearing contrast as in the weld produced using low axial force. Consistent with light microscopy observations, TEM observations of the weld zone at the outer periphery of the high axial force weld compared closely with the center of the weld produced at low axial force (Fig. 16C and D).

Compared to the similar-alloy IFR welds, TEM bright-field analysis of the homogeneous interface region at the center of the LFR weld (Fig. 17A and B) indicated a marked coarsening to sizes ranging from 120 to 1600 nm in length. While the finer dispersoids remained spherical, the coarser dispersoids experienced coarsening and elongation along the interface direction with an aspect ratio of approximately two. Despite this dispersoid coarsening, the alpha grain size in this region appeared equivalent to that of the base metal. Clusters of dispersoids present in the base metal

were not observed in this region, indicating their total break up. The inhomogeneous region outside of the central inner HDZ, where light-yellow contrast was observed in Fig. 12B, showed alternating deformed layers of fine dispersoids and deformed coarse dispersoids (Fig. 17B). Even though it was located at the boundary region, coarsening and deformation were noticeable, showing dispersoids ranging from 120 to 1350 nm in diameter. The interface region at the outer periphery showed a very similar microstructure but with slightly less-deformed, lower aspect ratio dispersoids (Figs. 17C). The asymmetric nature of the interface in the region observed on the light microscope was not discernible via TEM observation. The marked coarsening of dispersoids in the interface region originated from the slower thermal cycle experienced during the process and also the lesser extent of metal expulsion compared to the high axial force IFR weld. A higher axial force may be required to reduce the weld time and remove the dispersoid-coarsened region in the LFR welds.

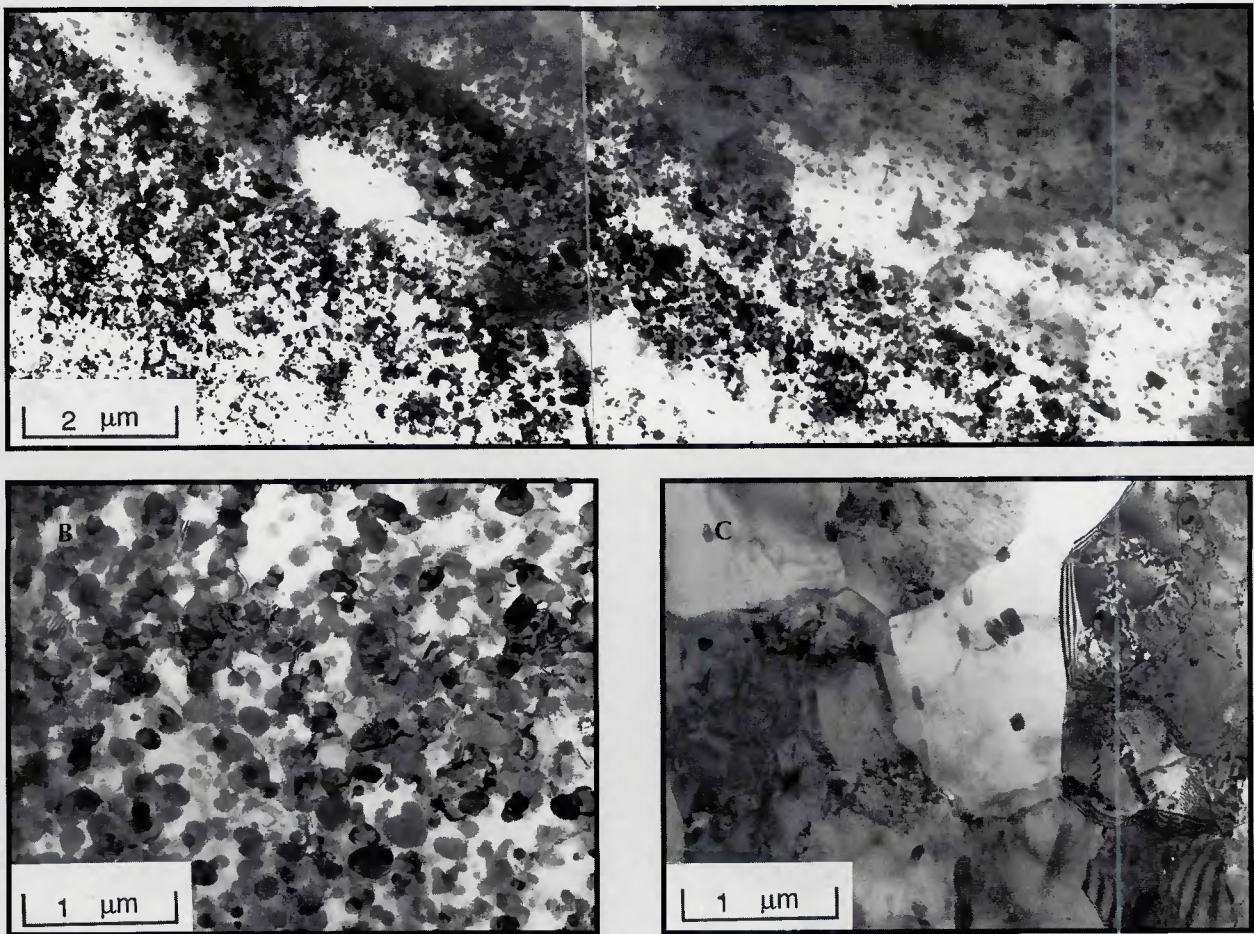


Fig. 18 — TEM bright-field micrographs of IFR welds produced between FVS1212 and 2024-T351 using high axial force. A — Overall view of the interface; B — FVS1212 near the interface; C — 2024-T351 near the interface.

#### Dissimilar-Alloy Welds

TEM bright-field micrographs of the dissimilar-alloy IFR weld produced using high axial force are shown in Fig. 18. Figure 18A shows the interface region at the axial centerline. Mechanical mixing between the two alloys is evident as penetrated layers of FVS1212 into the 2024-T351. Although deformation and mechanical mixing of the FVS1212 were observed near the interface, coarsening of the dispersoids was not apparent (Fig. 19B). Recrystallized 2024-T351 grains were nearly equiaxed and the alignment of intermetallic particles was not severe (Fig. 19C). The presence of S' precipitates was not observed indicating their reversion or solutionizing during the weld thermal cycle. The grain size of the recrystallized 2024-T351 ranged from 500 to 1000 nm. In the outer HDZ of the 2024-T351, the microstructure gradually changed from a fully recrystallized structure to a partially recrystallized subgrain structure with extensive dislocation tangles.

Coarse S' precipitates were not observed in this region, rather an absence of precipitates indicated their solutionizing or reversion. The outer periphery region showed essentially identical characteristics. TEM observation of the low axial force IFR weld showed features only slightly different from those of the high axial force IFR weld, and indicated a more abrupt transition across the interface with less mechanical mixing and slightly larger recrystallized grain size (500 to 1500 nm).

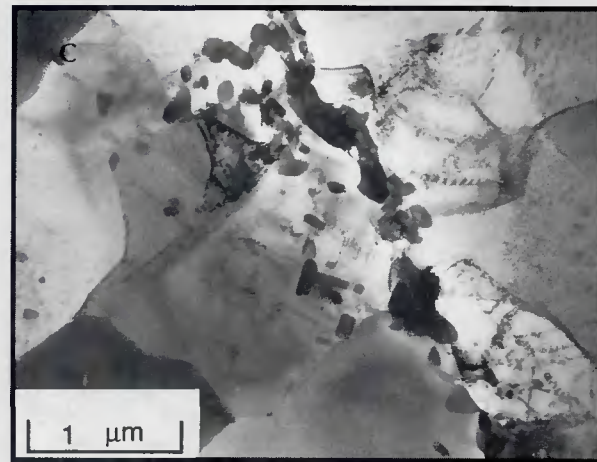
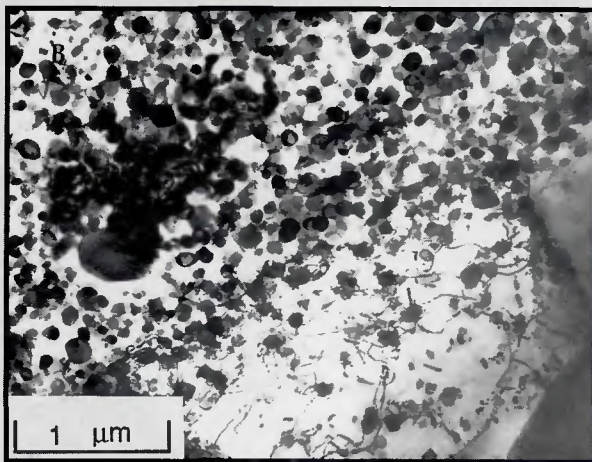
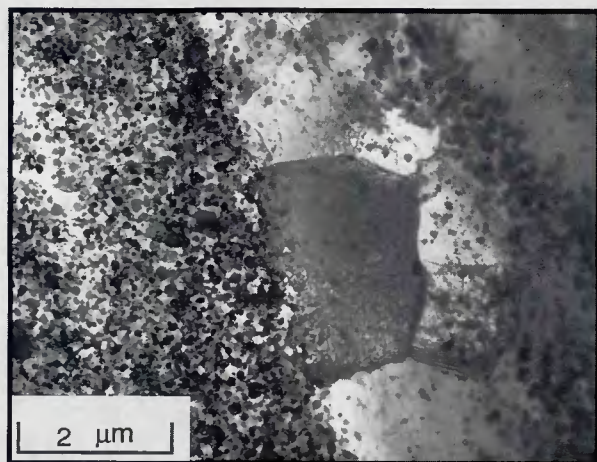
TEM bright-field micrographs of the dissimilar-alloy LFR welds (Fig. 19A–C) showed mechanical mixing between the two alloys only on a microscopic scale at the interface. The dispersoids within the FVS1212 showed no evidence of coarsening or deformation. Recrystallized 2024-T351 near the interface showed a wide range of alpha grain sizes with the grain boundary intermetallics aligned semicontinuously along the interface direction (Fig. 19C). The size of recrystallized grains ranged from 500 to 1500 nm.

#### Hardness Testing

##### Similar-Alloy Welds

Knoop microhardness traverses for the similar-alloy welds are shown in Figs. 9–11. Knoop hardness number (KHN) values across the outer HDZ at the axial centerline of the low axial force IFR weld (Fig. 9C) were equivalent to those in the base metal (KHN 183.5 in average, ranging from KHN 170 to 210), but decreased down to KHN 150 at the center of the inner HDZ. Interestingly, hardness variations in the HDZ were less than those observed in the unaffected base metal due to microstructural homogenization experienced in this region. The decrease in hardness within the inner HDZ was attributed to the marginal increase in dispersoid coarseness and alpha grain size. The hardness traverse at the outer periphery of this weld showed a similar trend, except within the dispersoid-lean white regions which exhibited a very low hardness down to about KHN 104. Hardness mea-

Fig. 19 — TEM bright-field micrographs of LFR welds produced between FVS1212 and 2024-T351. A, B — Overall view of the interface; C — 2024-T351 near the interface...



surements taken at the dark contrast regions adjacent to the dispersoid-lean bands exhibited a hardness of KHN 180, which was higher than the values at other regions of the inner HDZ.

Figure 10C shows the KHN hardness traverse across the interface of the similar-alloy high axial force IFR weld. Hard-

ness values were more uniform than across the base metal, and showed an increase to a maximum of KHN 210 in the inner HDZ. This increased hardness was attributed to the absence of dispersoid or grain coarsening in this region, and the breakup and redistribution of dispersoid clusters. A hardness traverse

across the outer periphery of the high axial force weld exhibited a consistent hardness of about KHN 175, which represented the lower end of the base metal hardness range. This slight loss of hardness was attributed to the homogenized but only slightly coarsened dispersoid structure in the region.

Table 2—Tensile Test Results for the Alloy/Process Combinations

Alloy/Process Combination	Spec Location	YS MPa (ksi)	TS MPa (ksi)	EL (%)	Joint Efficiency (%)	Fracture Location <sup>(a)</sup>
FVS1212	O.P. <sup>(b)</sup>	376 (55)	376 (55)	0.5	66	IHDZ
IFRW/L	Center	414 (60)	463 (67)	1.1	81	IHDZ
FVS1212	O.P.	415 (60)	487 (71)	2.1	85	IHDZ
IFRW/H	Center	418 (61)	482 (70)	1.6	84	IHDZ
FVS1212	O.P.	420 (61)	446 (65)	1.0	78	IHDZ
LFRW	Center	409 (59)	474 (69)	2.1	83	IHDZ
FVS1212/2024	O.P.	299 (43)	385 (56)	6.0	82	IHDZ/IF
IFRW/L	Center	319 (46)	376 (55)	1.7	80	IHDZ/IF
FVS1212/2024	O.P.	343 (50)	445 (65)	4.2	95	IHDZ/IF
IFRW/H	Center	328 (48)	443 (64)	4.5	95	IHDZ/IF
EVS1212/2024	O.P.	305 (44)	393 (57)	2.3	85	IHDZ/IF
LFRW	Center	314 (46)	409 (59)	2.6	87	IHDZ/IF
FVS1212 BM <sup>(c)</sup>		522 (76)	572 (83)	23.0		
2024-T351 BM <sup>(d)</sup>		324 (47)	469 (68)	20.0		

a IHDZ and IF denote inner heat- and deformation-affected zone and interface, respectively.

b O.P. denotes outer periphery.

c Ref. 1.

d Ref. 15.

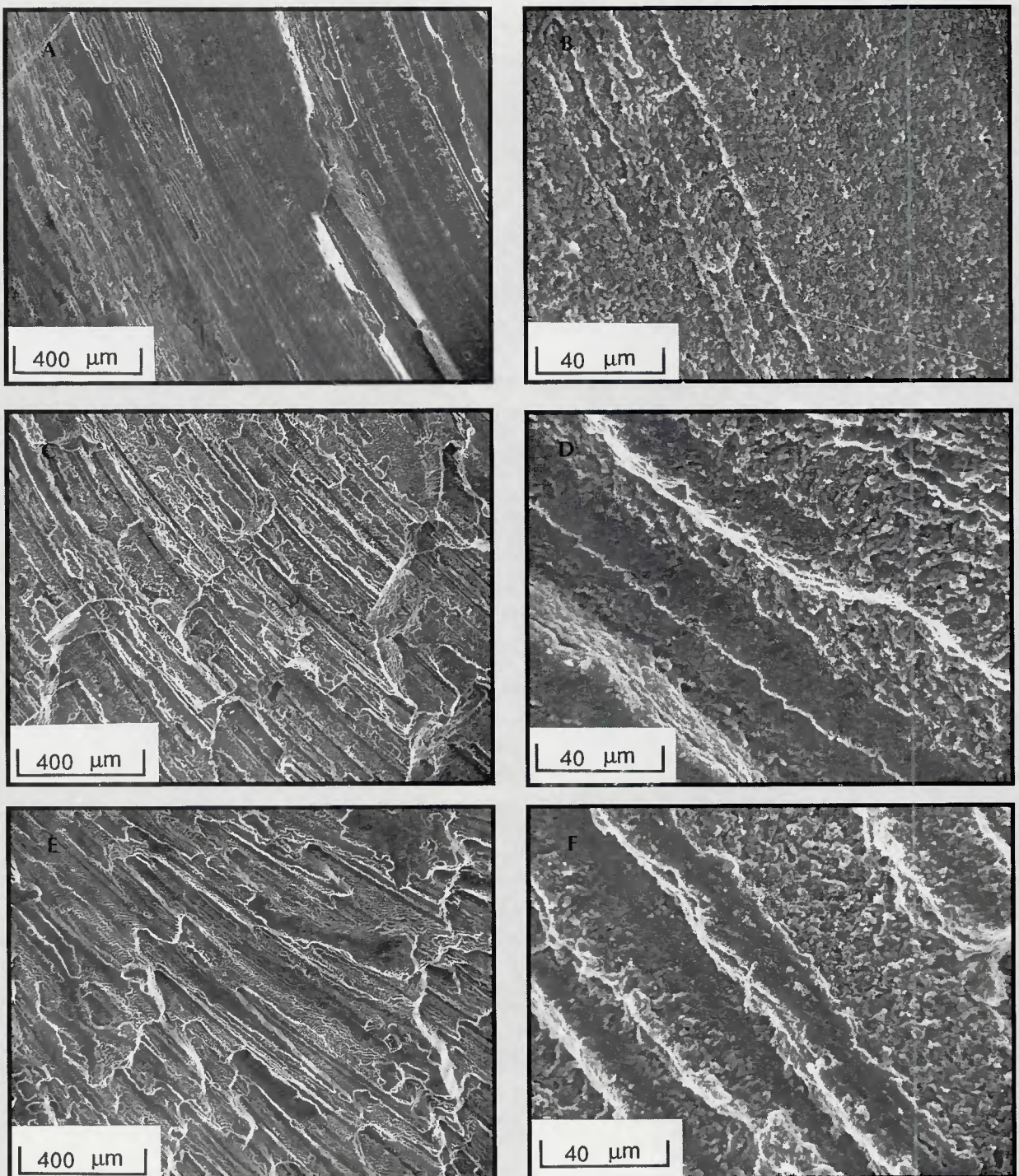


Fig. 20 — SEM fractographs of bend-test specimens extracted from similar-alloy welds in FVS1212. A, B — Inertia friction weld produced with low axial force; C, D — inertia friction weld produced with high axial force; E, F — linear friction weld.

Knoop microhardness traverses across the interface of the similar alloy FVS1212 LFR weld are shown in Fig. 11C. A noticeable hardness drop was observed within 200 microns of the interface at the axial center and within 500 microns at the outer periphery. The hardness drop at the interface region can be explained by the presence of coarsened

dispersoids in the region, as observed in Fig. 17B.

#### Dissimilar-Alloy Welds

Figures 13 and 14 compare the hardness traverses for the dissimilar alloy high axial force IFR and LFR welds. For both welds, the hardness in the FVS1212

remained constant across the region in accordance with TEM observations, which showed no microstructural changes. Both welds showed hardness variations in the inner and outer HDZs of the 2024-T351. For the high axial force IFR weld, hardness showed the lowest value (KHN 145 vs. 177 in the base metal) at the recrystallized inner

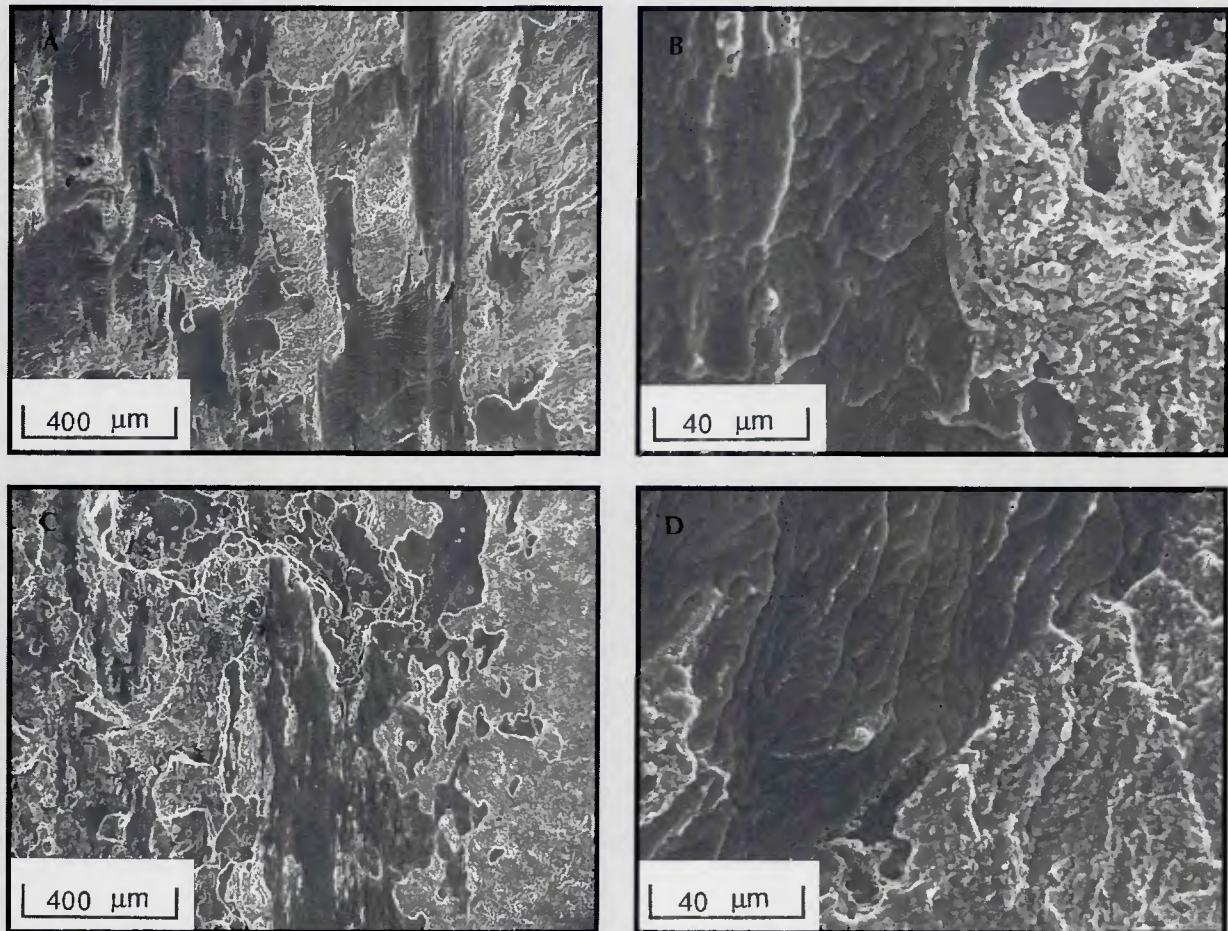


Fig. 21 — SEM fractographs of bend-test specimens extracted from dissimilar-alloy welds between FVS1212 and 2024-T351. A, B — Outer periphery of IFRW produced with low axial force; C, D — outer periphery of LFR weld.

HDZ, which gradually increased nearer to the base metal. It is suggested that the hardness drop in this region is related to recrystallization of the grain structure and solutionizing or reversion of the S' precipitates. Even with the extensive deformation in this region, work-hardening was apparently relieved by the recrystallization and recovery processes. The low axial force dissimilar-alloy IFR weld showed similar trends with slightly lower hardness values and wider regions of low hardness.

For the dissimilar-alloy LFR weld, the 2024-T351 HDZ region also showed decreased hardness values with a minimum value of KHN 130 — Fig. 14C. The lower hardness in the outer HDZ of this weld corresponded to a wider region of resolutionizing or reversion vs. the inertia friction welds, which was consistent with the wider total HDZ region observed macroscopically in Fig. 8.

#### Tensile Testing

Tensile testing results are shown in Table 2. The similar alloy low axial force

IFR weld in FVS1212 exhibited a joint efficiency of 81% at the axial centerline and 66% at the outer periphery. The appreciably lower joint efficiency at the outer periphery was attributed to the presence of soft, dispersoid-lean bands in the interface region at this location. Consistent with the microstructural and hardness test results, the similar-alloy higher axial force IFR weld exhibited higher tensile joint efficiencies of 84 and 85% at the axial centerline and outer periphery, respectively. The similar-alloy LFR weld in FVS1212 exhibited joint efficiencies at the axial centerline and outer periphery of 83 and 78%, respectively. These lower tensile strengths were attributed to greater coarsening of the dispersoids at the weld interface. Tensile fracture of all similar-alloy weld types occurred within the inner HDZ.

Dissimilar-alloy welds exhibited only slightly lower tensile strengths than the 2024-T351 base metal. Dissimilar-alloy IFR welds produced with high axial force showed the highest joint efficiencies of 95% both at the axial centerline and

outer periphery. Even with similar minimum hardness values at the inner HDZ as those in the high axial force IFR weld, a wider softened region in the low axial force weld promoted lower joint efficiencies of 80% at the axial centerline and 82% at the outer periphery. Despite exhibiting a relatively low hardness across a wide outer HDZ, the dissimilar-alloy LFR weld showed joint efficiencies of 87% at the axial centerline and 85% at the outer periphery, respectively.

#### Fracture Analysis

Scanning electron microscope (SEM) fractographs of bend and/or tensile test specimens are shown in Fig. 20 for similar-alloy welds in FVS1212 and in Figs. 21 and 22 for dissimilar-alloy welds between FVS1212 and 2024-T351.

#### Similar-Alloy Welds

SEM observation of bend test specimen fracture surfaces are shown in Fig.

20. Macroscopically, the IFR welds exhibited the typical, outwardly spiraled appearance indicative of the metal flow in the vicinity of the weld interface during welding. On a microscopic scale, fracture surfaces of the similar-alloy IFR welds produced using low axial force exhibited two fracture surface topographies. At some locations, a relatively flat, smooth surface was exhibited, as shown in Fig. 20A. Tear ridges separated regions of flat, nearly featureless fracture. Examination of these flat regions at high magnification (Fig. 20B) showed evidence of extremely fine dimples on the fracture surface. Other locations on the fracture surfaces of the low axial force IFR welds, and the entire surface of IFR welds produced using high axial force, exhibited more irregular fracture surface topographies, as shown in Fig. 20C. Small, flat regions which exhibited appreciable ductile fracture were separated by large tear ridges. As indicated above, both the direction of the tear ridges for both the low and high axial force welds followed an outwardly spiraled pattern. Analysis of the fracture surface at increased magnification (Fig. 20D) showed microvoids that had nucleated at the interface between the soft alpha-aluminum matrix and the hard dispersoid particles.

The fracture surface on the LFR weld specimen appeared similar to that of the high axial force inertia friction weld, except that the macroscopic flow pattern (*i.e.*, direction of the tear ridges) was nearly linear vs. the curvilinear pattern exhibited by the IFR welds.

#### Dissimilar-Alloy Welds

SEM fractographs of the dissimilar-alloy weld bend test specimens are shown in Fig. 21. Compared to the similar-alloy welds, the dissimilar-alloy welds exhibited similar, but less distinct macroscopic fracture patterns. On a microscopic scale, fracture surfaces in all welds exhibited two general features, flat, relatively smooth regions of dark contrast, and more irregular regions of light contrast. SEM analysis at increased magnification (Fig. 21B and D) and EDS analysis indicated that the flat regions were within the 2024-T351 inner HDZ directly adjacent to the weld interface and that the light-appearing regions were the FVS1212 inner HDZ. Interestingly, EDS analysis indicated that the dark-contrast 2024-T351 surfaces were slightly enriched in iron, while the light contrast FVS1212 regions contained both magnesium and copper, suggesting that fracture generally occurred at or very near to the weld interface where highly localized mechanical mixing or interdiffusion of the alloying elements

from the dissimilar base alloys had occurred. The examination of tensile specimen fracture surfaces in Fig. 22 for dissimilar-alloy IFR welds produced at low- and high axial force, and the LFR weld, showed similar fracture surfaces, with the low axial force weld exhibiting principally the smooth, dark contrast surface. The IFR weld produced at high axial force showed an increase in the proportion of light-contrast, more ductile-appearing fracture. The LFR weld exhibited a fracture surface pattern that appeared both macroscopically more ductile, but which on a microscopic scale also exhibited smooth surfaces of dark contrast and more ductile appearing surfaces of light contrast — Fig. 22F.

#### Welding Process and Parameter Effects

The purpose of the present investigation was to evaluate from a metallurgical perspective the feasibility of producing high-integrity welds in the RS/PM Al-Fe-V-Si alloy FVS1212 and between this alloy and the conventional aluminum alloy 2024-T351. Although the objective of this work was not to optimize process parameters, several important observations were made regarding the relationships between process parameters and weld characteristics.

In similar-alloy welds produced using the IFR welding process, axial force showed a significant effect on the weld upset, the presence of interface weld discontinuities, and the macro- and microstructures of the weld HDZ. The application of a higher axial force promoted a shorter weld cycle, greater axial upset and correspondingly a larger degree of flash expulsion, thereby resulting in the final bonding between metal interfaces which were less heat and deformation affected vs. the welds produced at low axial force. The LFR weld was produced at a force below that of both IFR welds and required a longer weld time (2 to 2.5 s vs. less than approximately 1 s for the IFR welds). The magnitude of upset and flash expulsion (which was determined principally by the preset level of axial upset during welding and the forge force) was intermediate between the low and high axial force IFR welds. It is anticipated that parameter optimization of the LFR welding process would include the application of a higher axial welding force to reduce the welding time (for the same preset axial upset distance) and possibly a higher forge force to promote greater expulsion of heat- and deformation-affected metal out of the weld interface region. Variations in the reciprocating frequency and amplitude may

also result in improved weld quality.

In the dissimilar-alloy friction welds, the lower elevated temperature strength of the 2024-T351 promoted deformation principally in this softer alloy with negligible deformation in the FVS1212. Macroscopic characteristics of the welds were comparable with the similar-alloy welds, with the LFR weld exhibiting intermediate upset and flash expulsion as compared to the low and high axial force IFR welds.

#### Structure/Property/Fracture Relationships

The expulsion of the heat- and deformation-affected metal from the interface of the similar-alloy high axial force IFR weld in FVS1212 promoted a weld interface that exhibited negligible dispersoid or alpha grain size coarsening vs. that of the base metal, and correspondingly, no hardness decrease across the interface. Indeed, the intense mechanical deformation experienced at the weld interface promoted homogenization of the base metal microstructure and an increase in hardness at the axial centerline. A slower weld thermal cycle and lower extent of interface expulsion, as in the low axial force IFR, did not significantly influence the interface structure at the axial centerline, but did promote nonhomogenous deformation at the outer periphery and the formation of soft, dispersoid-free zones in this region. Although not confirmed by fracture analysis, these zones likely contributed to the lower tensile strength measured in this region.

The comparatively longer LFR weld thermal cycle promoted noticeable coarsening of the dispersoid structure at the weld interface, and therefore, a softening of this region and decrease in joint efficiency vs. the IFR welds. As indicated above, an increase in the friction and forge forces during LFR welding would greatly decrease the welding time, increase expulsion and thereby promote the formation of a smaller HDZ at the weld interface.

It is of interest to note that despite noticeable softening and tensile fracture within the inner HDZ, particularly in the low axial force IFR and LFR welds, joint efficiencies remained relatively high. This may be attributed to the narrow width of these softened regions and reinforcement effects of the surrounding, higher-strength outer HDZ.

In both the IFR and LFR dissimilar alloy welds, a similar dynamically recrystallized, solutionized/reverted region was observed in the 2024-T351 side of the weld, which was consistent with the appreciably lower elevated

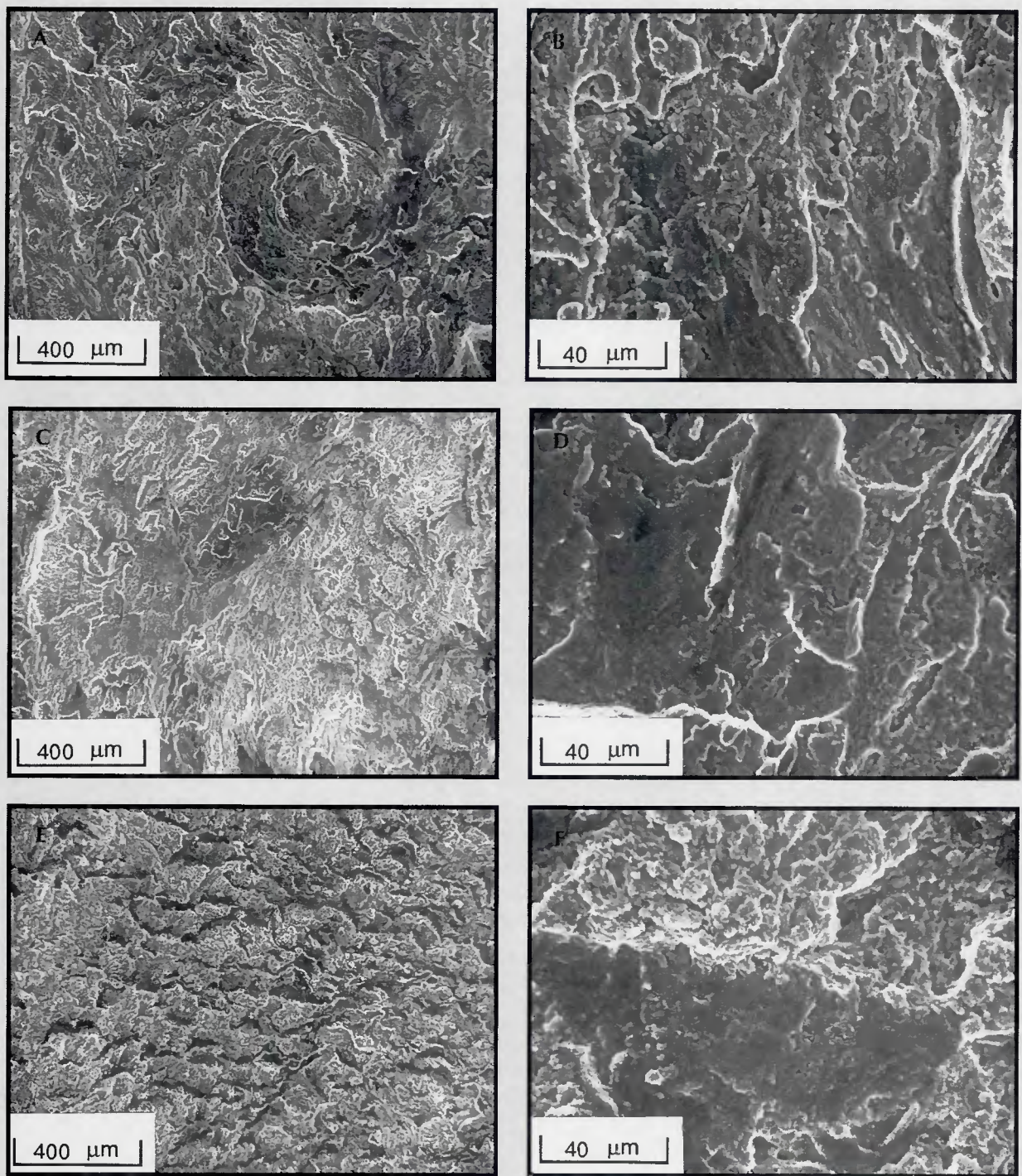


Fig. 22 — SEM fractographs of tensile test specimens extracted from dissimilar-alloy welds between FVS1212 and 2024-T351. A, B — Center of IFR weld produced with low axial force; C, D — center of IFR weld produced with high axial force; E, F — center of LFR weld.

temperature strength of this alloy vs. the FVS1212 and the rapid weld cooling rates. Both microstructure and fracture analysis indicated a greater extent of highly localized mixing between the base alloys at the weld interface with an increase in axial force. This increased intermixing may have contributed to the higher strength of the high axial force IFR weld and a greater extent of more ductile appearing fracture on the FVS1212 side of the interface. As in the similar alloy IFR welds, an increase in LFR welding force would be expected to promote greater interface mixing and higher joint efficiencies.

## Conclusions

1) The inertia and linear friction welding have been demonstrated to be effective processes for joining of RS/PM Al-Fe-V-Si alloys.

2) For similar-alloy inertia friction welds, a sufficiently high axial force was important in promoting a rapid thermal cycle and adequate expulsion of heat- and deformation-affected metal out of the weld interface. The weld region was characterized by negligible dispersoid and alpha grain coarsening, and correspondingly minimal hardness degradation, and a relatively high joint efficiency (about 85%).

3) A somewhat slower thermal cycle and less expulsion during the linear friction welding process promoted greater dispersoid coarsening and softening at the weld interface in similar alloy welds, and a lower joint efficiency averaging 81%. Optimization of welding parameters would be expected to reduce microstructural coarsening and increase joint efficiency.

4) Dissimilar inertia and linear friction welds were characterized by deformation nearly entirely in the 2024-T351. Despite appreciable metallurgical change in the 2024-T351 adjacent to the interface, the high axial force inertia friction weld and the linear friction weld exhibited relatively high joint efficiencies of 95 and 86%, respectively.

### Acknowledgments

The authors are indebted to Drs. S. K. Das and Paul Gilman of Allied-Signal, Inc., for providing the alloy evaluated in this study, Mr. I. Varol for color metallography and Dr. K. Sampath for his helpful comments. Appreciation is also expressed to Messrs. David Nicholas and Edward Watts of The Welding Institute, Cambridge, for performing linear friction welding trials. Finally, the authors are grateful to Drs. Andrew Crowsen and Edward Chen, and the Army Research Office, for providing financial support for this work under contract No. DAAL03-88-K-0049.

### References

1. High-Temperature Aluminum Alloy — FVS1212 and FVS0812 Data Sheet, Allied-Signal Inc., Morristown, N.J.
2. Das, S. K. and Davis, L. A. 1988. High-performance aerospace alloys via RS processing. *Materials Science and Engineering* 98: 1-12
3. Skinner, D. J. 1988. The physical metallurgy of dispersion strengthened Al-Fe-V-Si alloys. *Dispersion Strengthened Aluminum Alloys*. Y. W. Kim and W. M. Griffith, eds., TMS/AIME, Warrendale, Pa, pp. 181-197.
4. Bye, R. L., Kim, N. J., Skinner, D. J., Raybould, D., Brown, A. M. 1988. RS/PM aluminum alloys prepared from melt-spun ribbons. *Processing of Structural Metals by Rapid Solidification*, F. H. Froes and S. J. Sav-
- age, eds., ASM International, Metals Park, Ohio, pp. 283-289.
5. Krishnaswamy, S., and Baeslack, W. A. 1989. Structure, properties and fracture of pulsed Nd:YAG laser weld in Al-8Fe-2Mo. *Recent Trends in Welding Science and Technology* 89: 631. ASM International, Metals Park, Ohio.
6. Baeslack, W. A., and Krishnaswamy, S. 1986. Electron beam weldability of a rapidly solidified aluminum alloy. *Advances in Welding Science and Technology*, S. David, ed., ASM International, Metals Park, Ohio, p. 357.
7. Baeslack, W. A., Hou, K. H. and Develian, J., 1988. Rapid solidification joining of a powder metallurgy Al-Fe-Ce alloy. *J. Mat. Sci. Lett.* 7: 947
8. Baeslack, W. A., and Hou K. H. 1989. Electron microscopy of rapidly solidified weldments in a powder metallurgy Al-Fe-Ce alloy. *J. Mat. Sci. Lett.* 8: 2642-2653
9. Ananthanarayanan, V. 1988. Diffusion Welding of an RS/PM aluminum alloy. Ph.D. dissertation, The Ohio State University, Columbus, Ohio.
10. Baeslack, W. A., and Hagey, K. S. 1988. Inertia friction welding of rapidly solidified powder metallurgy aluminum. *Welding Journal* 67(7): 139-s.
11. Hou, K. H., and Baeslack, W. A. 1990. Electron microscopy of inertia friction weldments in a rapidly solidified Al-Fe-Mo-V alloy. *J. Mat. Sci.* 25: 2642-2653
12. Koo, H. H., Krishnaswamy, S. and Baeslack III, W. A. 1991. Structure, properties and fracture relationships in inertia friction weldments between a rapidly-solidified Al-Fe-Mo-V and IM 2024-T351. *J. Mat. Sci.* (in review).
13. Nicholas, E. D. 1987. Friction welding non-circular sections with linear motion — a preliminary study, Cambridge, England, The Welding Institute.
14. Aluminum: Properties and Physical Metallurgy. 1984. J. F. Hatch, ed., ASM International, Materials Park, Ohio, p. 78.
15. Metals Handbook Vol. 2, 10th Edition. 1990. ASM International, Materials Park, Ohio, pp. 71 and 628.

## CORRECTION

The paper, "Mechanical Properties of Flux Cored Iron-Manganese-Aluminum Weld Metal," by K. Makhamreh and D. Aidun, was published in the March 1992 Research Supplement. Table 6, which appeared on Page 109-s, contained an error in the heading of the second column. The corrected table appears at right.

**Table 6 — Transverse Microhardness Measurements of the Weld Metals (300g – DPH)**

Weld Metal <sup>(a)</sup>	M(DPH) <sup>(b)</sup>	S <sup>(c)</sup>	R <sup>(d)</sup>
I	203	12.5	49
II	271	11.0	44
III	240	11.5	41
IV	306	17.8	68
V	253	11.6	33
VI	284	15.1	51
310	268	16.6	70
316	272	11.8	46

(a) 19 data points.

(b) M — Mean.

(c) S — Standard

(d) R — Range.

# WRC Bulletin 345

## July 1989

### Assessing Fracture Toughness and Cracking Susceptibility of Steel Weldments—A Review

By J. A. Davidson, P. J. Konkol and J. F. Sovak

The literature survey reviews the domestic and foreign literature to determine, document and evaluate: 1) the parameters of welding that control weld-metal and HAZ cracking; 2) tests for assessing the susceptibility of structural steel to weld-metal and HAZ cracking; 3) the parameters of welding that control HAZ toughness; and 4) tests for measuring the toughness of weld metal and HAZ. The work was performed at the United States Steel Corporation Technical Center in Monroeville, Pa., and was sponsored by the Offices of Research and Development, Federal Highway Administration, U.S. Department of Transportation, Washington, D.C.

Publication of this bulletin was sponsored by the Weldability Committee of the Welding Research Council. The price of WRC Bulletin 345 is \$30.00 per copy, plus \$5.00 for U.S. and \$10.00 for overseas, postage and handling. Orders should be sent with payment to the Welding Research Council, Room 1301, 345 E. 47th St., New York, NY 10017.

# WRC Bulletin 347

## September 1989

This bulletin contains two reports:

### (1) Welded Tees Connections of Pipes Exposed to Slowly Increasing Internal Pressure

By J. Schroeder

### (2) Flawed Pipes and Branch Connections Exposed to Pressure Pulses and Shock Waves

By J. Schroeder

Publication of these reports was sponsored by the Subcommittee on Reinforced Openings and External Loadings of the Pressure Vessel Research Committee of the Welding Research Council. The price of WRC Bulletin 347 is \$25.00 per copy, plus \$5.00 for U.S. and \$10.00 for overseas, postage and handling. Orders should be sent with payment to the Welding Research Council, Room 1301, 345 E. 47th St., New York, NY 10017.

## WANTED – MEMBERS FOR THE SUBCOMMITTEE ON NICKEL ALLOYS

This committee will prepare a series of documents to provide recommended practices for joining all types and forms of nickel alloys. Initially, the Subcommittee will prepare a guide to welding the wrought forms of solid solution nickel alloys. Later documents will cover cast nickel alloys and age-hardening nickel alloys. The documents will describe the alloys and give typical uses, material preparation, joint designs, joining parameters, postweld treatment, and preparations. All forms of arc welding, electron and laser beam welding will be included in each document. Persons interested in working with the Subcommittee should contact:

R. L. O'Brien  
AWS Headquarters  
800 443-9353, Ext. 297